Spectroscopy®

Solutions for Materials Analysis

April 2017 Volume 32 Number 4 www.spectroscopyonline.com

Volumetric QC Analysis of Pharmaceuticals with Transmission Raman Spectroscopy

Data Governance at the Laboratory Level

How Pump–Probe Microscopy Advances Spectroscopic Imaging

Using IR Spectra to Identify Alcohols

UBM

GET MORE SPECTRAL DATA IN LESS TIME

The Ocean FX Spectrometer Offers Fast Acquisition Speed, Robust Communications and Spectral Buffering

FAST ACQUISITION SPEED

Acquire and process more spectral data in less time

Ideal for high speed testing and reaction monitoring

ROBUST INTERFACE

Operates via Gigabit Ethernet, Wi-Fi and USB

Use flexible instruments for QC and process monitoring

SPECTRAL BUFFERING

Onboard buffer holds up to 50,000 spectra so you don't miss a single data point

Ensures data integrity in applications such as chemical kinetics

Ocean Optics

info@oceanoptics.com • www.oceanoptics.com • **US** +1 727-733-2447
EUROPE +31 26-3190500 • **ASIA** +86 21-6295-6600

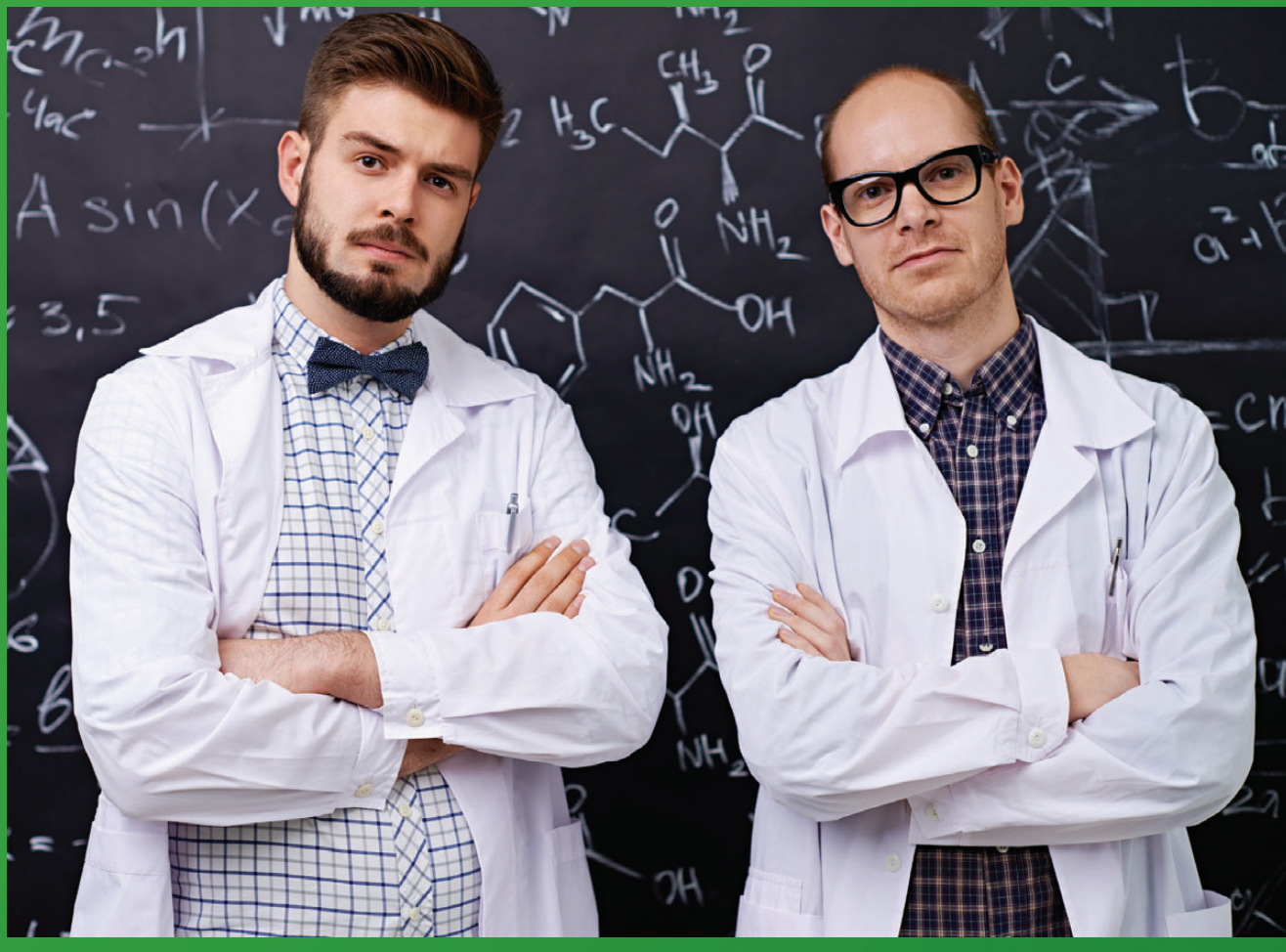

MAKE NO MISTAKE IT'S UV THAT EVERYONE CAN USE

New materials testing, R&D, analytical testing – your challenges are getting more complex all the time. So the answer is UV systems that are easy to learn *and* use. With LAMBDA™, your scientists can *quickly* become confident UV/Vis users – and that means more confidence in their results. And with automatic accessory alignment capability, those results can be virtually mistake-free.

LAMBDA systems: There's no mistaking the UV/Vis leader.

LAMBDA 265/3 65/465 UV/Vis Systems

www.perkinelmer.com/UVVisSolutions

PerkinElmer®
For the Better

Spectroscopy®

MANUSCRIPTS: To discuss possible article topics or obtain manuscript preparation guidelines, contact the editorial director at: (732) 346-3020, e-mail: Laura.Bush@ubm.com. Publishers assume no responsibility for safety of artwork, photographs, or manuscripts. Every caution is taken to ensure accuracy, but publishers cannot accept responsibility for the information supplied herein or for any opinion expressed.
SUBSCRIPTIONS: For subscription information: *Spectroscopy,* P.O. Box 6196, Duluth, MN 55806-6196; (888) 527-7008, 7:00 a.m. to 6:00 p.m. CST. Outside the U.S., +1-218-740-6477. Delivery of *Spectroscopy* outside the U.S. is 3–14 days after printing. Single-copy price: U.S., $10.00 + $7.00 postage and handling ($17.00 total); Canada and Mexico, $12.00 + $7.00 postage and handling ($19.00 total); Other international, $15.00 + $7.00 postage and handling ($22.00 total).
CHANGE OF ADDRESS: Send change of address to *Spectroscopy,* P.O. Box 6196, Duluth, MN 55806-6196; provide old mailing label as well as new address; include ZIP or postal code. Allow 4–6 weeks for change. Alternately, go to the following URL for address changes or subscription renewal: http://ubmsubs.ubm.com/?pubid=SPEC
RETURN ALL UNDELIVERABLE CANADIAN ADDRESSES TO: IMEX Global Solutions, P.O. Box 25542, London, ON N6C 6B2, CANADA. PUBLICATIONS MAIL AGREEMENT No.40612608.
REPRINT SERVICES: Reprints of all articles in this issue and past issues are available (500 minimum). Call 877-652-5295 ext. 121 or e-mail bkolb@wrightsmedia.com. Outside US, UK, direct dial: 281-419-5725. Ext. 121
C.A.S.T. DATA AND LIST INFORMATION: Contact Ronda Hughes, (218) 464-4430; e-mail: Ronda.Hughes-Stovern@ubm.com
INTERNATIONAL LICENSING: Maureen Cannon, (440) 891-2742, fax: (440) 891-2650; e-mail: Maureen.Cannon@ubm.com

50% Recycled Paper 10-20% Post Consumer Waste

Alliance for Audited Media

Connectiv

Ultra High Performance Silicon Drift Detectors

New! FAST SDD®

Count Rate = >1,000,000 CPS

The True State-of-the-Art

25 mm² FAST SDD® ^{55}Fe Spectrum

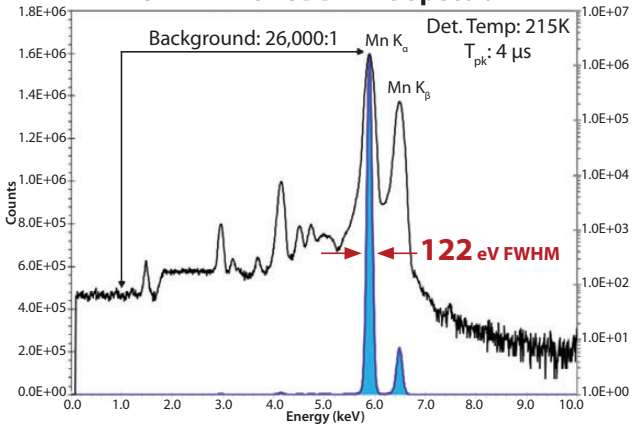

Resolution vs Peaking Time

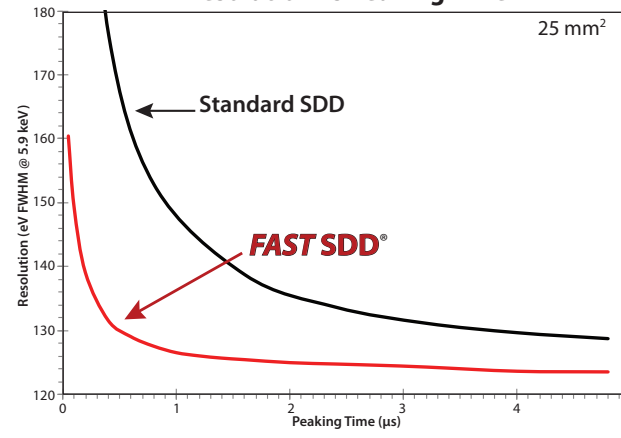

- **Lower noise** ⇨ Resolution down to 122 eV FWHM
- **Lower leakage current** ⇨ Higher temperature operation
- **Improved charge collection** ⇨ Better photopeak shape (no tailing)
- **New in-house manufacturing** ⇨ Consistent performance

Options:

- 25 mm² collimated to 17 mm²
- 70 mm² collimated to 50 mm²
- Windows: Be (0.5 mil) 12.5 µm, or C Series (Si3N4)
- TO-8 package fits all Amptek configurations

X-Ray Spectrometer

XRF System

OEM Components for XRF

XRF Experimenter's Kit

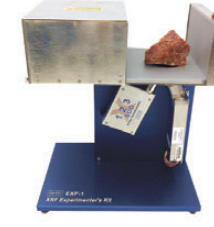

OEM's #1 Choice for XRF

AMPTEK Inc.
www.amptek.com

AMETEK®
MATERIALS ANALYSIS DIVISION

Spectroscopy®

485F US Highway One South, Suite 210
Iselin, NJ 08830
(732) 596-0276
Fax: (732) 647-1235

Michael J. Tessalone
Vice President/Group Publisher
Michael.Tessalone@ubm.com

Edward Fantuzzi
Publisher
Edward.Fantuzzi@ubm.com

Stephanie Shaffer
Associate Publisher
Stephanie.Shaffer@ubm.com

Michael Kushner
Senior Director, Digital Media
Michael.Kushner@ubm.com

Laura Bush
Editorial Director
Laura.Bush@ubm.com

Megan L'Heureux
Managing Editor
Meg.L'Heureux@ubm.com

Stephen A. Brown
Group Technical Editor
Stephen.Brown@ubm.com

Cindy Delonas
Associate Editor
Cindy.Delonas@ubm.com

Kristen Moore
Webcast Operations Manager
Kristen.Moore@ubm.com

Vania Oliveira
Project Manager
Vania.Oliveira@ubm.com

Sabina Advani
Digital Production Manager
Sabina.Advani@ubm.com

Kaylynn Chiarello-Ebner
Managing Editor, Special Projects
Kaylynn.Chiarello.Ebner@ubm.com

Dan Ward
Art Director
dward@hcl.com

Anne Lavigne
Marketing Manager
Anne.Lavigne@ubm.com

Ronda Hughes
C.A.S.T. Data and List Information
Ronda.Hughes-Stovern@ubm.com

Wright's Media
Reprints
bkolb@wrightsmedia.com

Maureen Cannon
Permissions
Maureen.Cannon@ubm.com

Jesse Singer
Production Manager
jsinger@hcl.com

Wendy Bong
Audience Development Manager
Wendy.Bong@ubm.com

Matt Blake
Audience Development Assistant Manager
Matt.Blake@ubm.com

MOXTEK®
INNOVATING SOLUTIONS

The Moxtek ICE Cube™ Polarizing Beamsplitter

Matthew George, PhD, Moxtek

Moxtek's ICE Cube™ polarizing beam splitter was developed for applications requiring large cone angles while maintaining color uniformity and image contrast over the visible wavelength spectrum. Applications where this advantage is important include: Head Mounted Display (HMD), Head-Up Display (HUD), and sensitive imaging systems.

Cube beamsplitters are found in a variety of spectroscopic applications where matching path lengths, reduced ghosting, and limited beam shift are important. Polarizing beamsplitter cubes are found in phase-shifting laser interferometers, polarization sensitive optical coherence tomography, and polarization sensitive white light interferometry. PBS cubes are often used for applications that require compact designs and reduced mechanical vibration. Typically MacNeille cubes have been used for many PBS applications, but for low f/#'s (large cone angles), the color balance and the contrast ratio between passing and blocking state transmittance have been less than ideal. On the contrary, wire grid polarizers (WGP) are known for excellent broadband performance in low f/# applications. By incorporating a WGP along the hypotenuse of a cube beamsplitter, the Moxtek ICE Cube provides a superior PBS in low f/# applications.

Experimental Conditions

As depicted in Figure 1a, a white light LED source was collimated and passed through an iris followed by a high contrast pre-analyzer to select an input polarization state. The beam was then focused into Moxtek and MacNeille Cube beamsplitters and the blocking state transmittance (T_s) was minimized on a screen. The blocking state reflectance and transmittance were then imaged using a camera, as was the passing state transmittance and reflectance (after rotating pre-analyzers by 90°). In both cases the aperture was varied to change the f/#, and the images were taken at about f/1.2 cone angle.

Results

As shown in Figure 1, the ICE Cube (Figure 1c) has improved color balance and a reduced leakage in the blocking state (T_s) when compared to the MacNeille cube (Figure 1b). Both cubes were also characterized at variable angles with well collimated light from the UV to the SWIR. The Moxtek

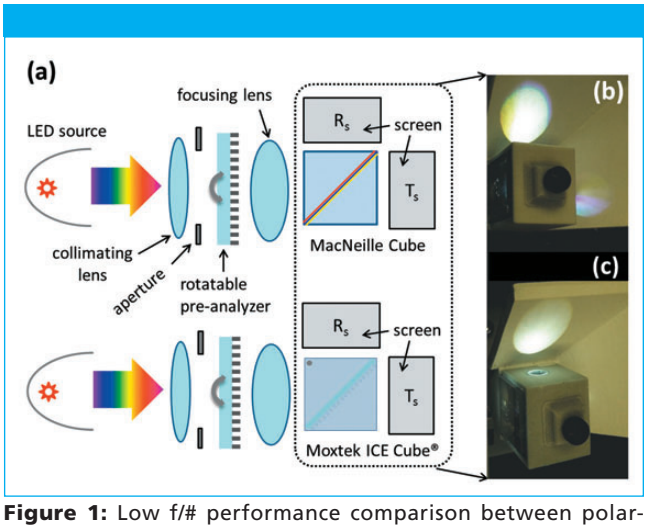

Figure 1: Low f/# performance comparison between polarizing beam splitter cubes. Measurement schematic (a) and results (b–c) showing blocking state transmittance (T_s) and reflectance (R_s) for MacNeille Cube (b) and Moxtek ICE Cube (c).

ICE Cube outperformed the MacNeille cube, accommodating angular deviations from normal incidence of ±20° in the azimuthal direction and ±10° in the polar (elevation) direction with minimal performance variation.

Conclusions

The Moxtek ICE Cube beamsplitter with embedded nanowire grid polarizer provides superior broadband performance over a wide angular aperture, with none of the dramatic color shifts and angular performance variations evident in MacNeille cube beamsplitters. While MacNeille cube designs can typically only tolerate a narrow angular aperture before performance deteriorates, the Moxtek ICE Cube accommodates a much larger angular field of view, allowing the optical designer to maintain system performance in broadband spectroscopic applications with demanding form factors.

Moxtek, Inc.
452 West 1260 North, Orem, UT 84057
tel. (801) 225-0930, fax (801) 221-1121
Website: www.moxtek.com

Spectroscopy

April 2017
Volume 32 Number 4

Cover image courtesy of Planar / shutterstock.

ON THE WEB

WEB SEMINARS

Raman Spectroscopy and Photoluminescence of Defects and Impurities in Crystals
David Tuschel, Horiba

Identification of Unknowns Using Raman Spectroscopy
Gregory M. Banik, PhD, Bio-Rad

Advanced Interference Removal Using ICP-MS with Triple Quadrupole Mass Spectrometry
Shona McSheehy, PhD, and Dr. Daniel Kutscher, PhD, Thermo Fisher Scientific

Updated European Standards for Water Analysis Using ICP-MS
Patrick Thomas, PhD, Emeritus Senior Scientist in Analytical Chemistry and Jean-Pierre Lener, Agilent Technologies, Inc.

http://www.spectroscopyonline.com/SpecWebSeminars

Like *Spectroscopy* on Facebook:
www.facebook.com/SpectroscopyMagazine

Follow *Spectroscopy* on Twitter:
https://twitter.com/spectroscopyMag

Join the *Spectroscopy* Group on LinkedIn
http://linkd.in/SpecGroup

CONTENTS

VOLUME 32 NUMBER 4
APRIL 2017

COLUMNS

PEER-REVIEWED ARTICLES

INTERVIEWS

DEPARTMENTS

Spectroscopy (ISSN 0887-6703 [print], ISSN 1939-1900 [digital]) is published monthly by UBM Life Sciences 131 West First Street, Duluth, MN 55802-2065. *Spectroscopy* is distributed free of charge to users and specifiers of spectroscopic equipment in the United States. *Spectroscopy* is available on a paid subscription basis to nonqualified readers at the rate of: U.S. and possessions: 1 year (12 issues), $74.95; 2 years (24 issues), $134.50. Canada/Mexico: 1 year, $95; 2 years, $150. International: 1 year (12 issues), $140; 2 years (24 issues), $250. Periodicals postage paid at Duluth, MN 55806 and at additional mailing offices. POSTMASTER: Send address changes to *Spectroscopy*, P.O. Box 6196, Duluth, MN 55806-6196. PUBLICATIONS MAIL AGREEMENT NO. 40612608, Return Undeliverable Canadian Addresses to: IMEX Global Solutions, P. O. Box 25542, London, ON N6C 6B2, CANADA. Canadian GST number: R-124213133RT001. Printed in the U.S.A.

ANY MATRIX
ANY INTERFERENCE
ANY PARTICLE SIZE

NexION 2000 ICP-MS: Triple quad power meets single quad versatility.

Trace metals in food, nanomaterials in water, impurities in everything from pills to electronic components: These are the sweet spot for the NexION® 2000 ICP-MS. Its sample introduction technology lets you run samples with up to 35% total dissolved solids. Plus, its interference removal capabilities give you the best detection limits for your application. And it delivers superior analysis times and single particle/cell detection capability – at least 10x faster than competitive systems. So the NexION 2000 ICP-MS is up to the most important challenge of all: ***Yours.***

For more information,
visit perkinelmer.com/NexION2000

NexION 2000 ICP Mass Spectrometer

PerkinElmer®
For the Better

Editorial Advisory Board

Spectroscopy's Editorial Advisory Board is a group of distinguished individuals assembled to help the publication fulfill its editorial mission to promote the effective use of spectroscopic technology as a practical research and measurement tool. With recognized expertise in a wide range of technique and application areas, board members perform a range of functions, such as reviewing manuscripts, suggesting authors and topics for coverage, and providing the editor with general direction and feedback. We are indebted to these scientists for their contributions to the publication and to the spectroscopy community as a whole.

News Spectrum

New ASTM Method Uses ICP–AES to Determine Aluminum Alloy Composition

ASTM's committee on analytical chemistry for metals, ores, and related materials has developed a new method for analyzing the composition of aluminum and aluminum alloys. The test will help manufacturers, consumers, and laboratories verify that an alloy's composition is within the needed limits through inductively coupled plasma–atomic emission spectrometry (ICP-AES). This method will soon be published as E3061, Test Method for Analysis of Aluminum and Aluminum Alloys by Inductively Coupled Plasma Atomic Emission Spectrometry (Performance Based Method).

The new method is performance based, but it also provides established preparation and analysis techniques. Additionally, the standard establishes expected repeatability of this method.

"The composition of an aluminum alloy is one factor that determines the final properties of the metal, such as strength, hardness, and durability," said ASTM member Jeneé Jacobs. He noted that ICP-AES is currently being used in many laboratories as a replacement for wet chemistry techniques and other outdated analytical methods. ■

IR QUIZ TIME

The infrared spectrum for your next interpretation exercise is shown in the figure below. Using the information provided here and what you have learned from previous columns, try to determine the complete chemical structure of this pure compound.

At minimum, try to determine whether this is an alcohol, and if it is, what type it is. Here's a hint: Assume the 2965 and 2938 peaks are the same size. They might not appear so due to a plotting error.

Table #: Assignments for new problem spectrum

Peaks	Assignments
3342	?
2965	?
2938	?
2879	?
1461	?
1385	?
1058	?
969	?
889	?
660	?

To see the answer, please turn to page 20 in this issue.

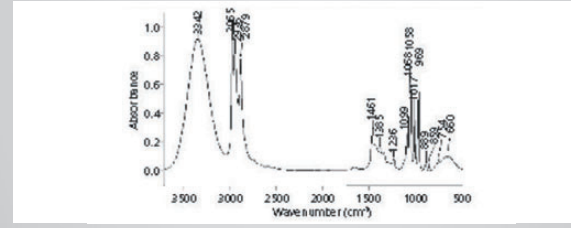

The IR spectrum of a liquid. Sampling method: capillary thin film.

http://www.spectroscopyonline.com/ir-spectral-interpretation-workshop-quiz-9

MARKET PROFILE: ENVIRONMENTAL AND FOOD APPLICATIONS FORGING GROWTH FOR ICP AND ICP-MS

Inductively coupled plasma (ICP) and ICP–mass spectrometry (ICP-MS) is mainly used for materials analysis applications for the determination of metals in the parts-per-billion and parts-per-trillion range, respectively. ICP and ICP-MS will work alongside with an atomic absorption (AA) spectrophotometer, where the ICP system has the advantage for delivering multielement analysis, and AA is preferred when fewer than 10 elements need to be analyzed.

Although weakness in the metals and mining industry has challenged the market for spectroscopy instruments in 2016, the demand for environmental and food testing have been robust, forging growth for key technologies such as ICP and ICP-MS. The Food and Agricultural Organization (FAO) and World Health Organization (WHO) continue to develop methods and standards to monitor toxic materials that could potentially enter the food chain through industrial pollution or environmental contamination.

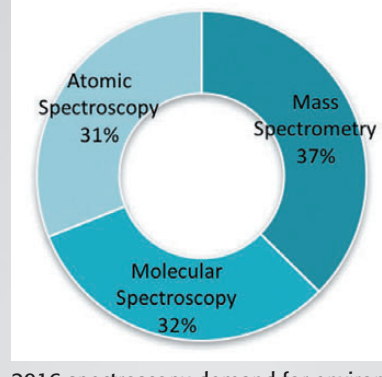

2016 spectroscopy demand for environmental and food applications.

In particular, demand for ICP-MS has been strong fueled by testing of soil, rice products, apple juice, drinking water, and seafood, among other foods. ICP-MS can simultaneously determine trace levels of contaminants or toxins such as arsenic, cadmium, chromium, lead, and mercury. Rice and rice-based foods, for example, accumulate the highest level of arsenic among food crops. Rice is the staple of many Asian countries, and its consumption continues to rise in Africa and South America.

ICP and ICP-MS accounts for 15% of the market for spectroscopy techniques used in environmental and food applications. The market is led by Agilent, PerkinElmer, and Thermo Fisher Scientific. Overall growth is forecasted to be strong over the next several years as laboratories continue to welcome new high-end instruments such as Agilent's 8900 ICP-QQQ and Thermo Fisher Scientific's iCAP TQ triple-quad ICP-MS systems into their research and testing facilities.

Spectroscopy techniques, including mass spectrometry, molecular spectroscopy, and atomic spectroscopy, are important tools that help monitor the environment and ensure the safety of the world's foods. Combined, these technologies represent nearly two billion dollars in instrument sales annually.

Market size and growth estimates were adopted from TDA's Industry Data, a database of market profiles from independent market research firm, Top-Down Analytics. For more information, contact Glenn Cudiamat, General Manager at (888) 953-5655 or glenn.cudiamat@tdaresearch.com. Glenn is a market research expert and has been covering the analytical instrumentation industry for nearly two decades.

Focus on Quality

Understanding Data Governance, Part II

Data integrity requires a multilayered approach that runs throughout a regulated organization. Here we discuss the laboratory level.

R.D. McDowall

In the first part of this series (1), I spoke about data governance at the corporate level. For the second part, I will focus on the laboratory and discuss the impact of the data governance scheme as it cascades down to the processes and systems at the bench.

Line management will be responsible for ensuring that the corporate policies and procedures as well as the requirements for an open culture are communicated down the line to the operational staff as outlined in Table II in Part I. My main focus here will be on data ownership and data stewards because the Internation Society of Pharmaceutical Engineering (ISPE) paper only has a single passing reference to data owners (2), but data ownership is mentioned in the Medicines and Healthcare Products Regulatory Agency (MHRA) and World Health Organization (WHO) data integrity guidance documents (3,4).

How do we get from data governance to data ownership? The WHO data integrity guidance (4) states in Section 4.10, "To ensure that the organization, assimilation, and analysis of data into a format or structure that facilitates evidence-based and reliable decision making, data governance should address data ownership and accountability for data process(es) and risk management of the data life cycle."

As we can see, a part of data governance is data ownership and accountability for data processes and associated risk management in any data life cycle. Since we are dealing with spectroscopic analysis, we will focus on computerized systems that control a spectrometer. However, do not forget any manual processes in your laboratories that also need assurance of the integrity of records generated.

How do we know who are data owners, and what are their responsibilities? The guidance documents are not much help here, so let's return to the definitions of data governance in Table I from Part I for some assistance. The nonpharmaceutical definitions listed in the right-hand column show that data governance focuses on defining the rules, roles, and responsibilities for acquisition and management of data. In my opinion, data owners should be responsible for these functions because they should know the process that is automated by the spectrometer. However, there are already two roles for a computerized system defined in *Good Automated Manufacturing Practice (GAMP) 5* (5) and *Annex 11* (6): the process owner and the system owner. These two roles were originally defined in *GAMP 5* (5) and were simplified in *Annex 11* (6) as follows:

Process owner:

- The person ultimately responsible for the business process or processes being managed (5).
- The person responsible for the business process (6).

System owner:

- The person ultimately responsible for the availability, support, and maintenance of a system, and for the security of the data residing on the system (5).
- The person responsible for the availability and maintenance of a computerized system and for the security of the data residing on that system (6).

These are the two roles that are defined in the regulations. The split in responsibilities above gives rise to the concept of process owner in the business and system owner in IT. Note that for stand-alone systems, the two sets of re-

sponsibilities are merged and the process owner is also the system owner. Hands up for those lucky individuals in this situation!

Can a Process Owner Be a Data Owner?

How should these regulatory roles fit within a data governance framework? Let's start with the data owner. The obvious fit is for the process owner to be the data owner as well because data are generated and converted to information in the business. Therefore, we could modify the *Annex 11* definition of process owner and encompass data ownership as follows: "The person responsible for the business process including the data generated, transformed, and reported by a manual process or a computerized system."

So, who should be a process or data owner? *GAMP 5* gives some guidance that is self-explanatory (5): "This person is usually the head of the functional unit or department that uses the system, although the role should be based on specific knowledge of the process rather than position in the organization."

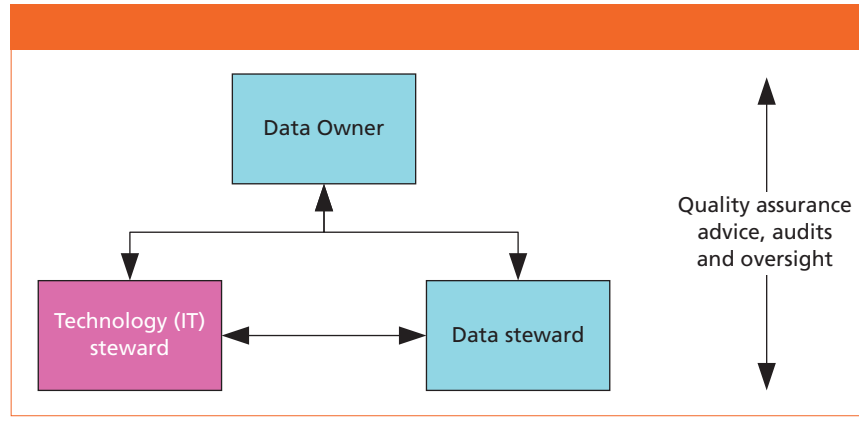

Figure 1: Data governance at the process and system level.

One potential area of confusion concerns the name "data owner," which implies that an individual owns the date rather than the organization that owns the system and the data generated by it. That situation is not so—the organization owns the data, and the data owner is merely the custodian of the data in the system who acts on behalf of the organization. Perhaps *data custodian* may be a better title for this individual.

Other Data Governance Roles at the System Level

We will look in some more detail within our regulated analytical laboratory at the other roles involved in data ownership. In addition to the data owner, there are two other roles as follows:

Table I: Process and system level roles and responsibilities

Role	Responsibilities
Data owner	• Implements directives and procedures from the corporate data governance steering committee • Responsible for one or more workflow processes that may be manual, hybrid or electronic or a combination of all three • Risk assessment of the processes and systems to determine record vulnerability • Remediation efforts in the short term to fix record vulnerability and a longer term fix for business benefit • Approves, modifies or rejects all data governance requests with the process or system for which they are responsible • Defines and authorizes the data quality, integrity and security of the process • Defines and authorizes the record security, user roles, and access privileges of computerized systems • Defines the data backup and recovery for computerized systems • Reporting to the data governance steering committee on progress of work and process and system metrics
Data steward	• Implements data owner's requirements for the process and systems • Ensure and helps users to follow the security, data quality and data integrity requirements implemented in the system or process • Review data generated by users using the system and process • Coordinate IT activities for supporting networked systems • Identify improvement ideas for discussion with the data owner • Generate metrics for the data owner to report
Technology steward	• Ensure that the computer platform is adequate for data integrity needs defined by the data owner • Support computerized systems that create, process, report, and store data • Configure the application to meet the data owner's specifications • Granting, modifying and revoking user access following receipt of a request from the data owner • Backup and recovery of data on computerized systems according to the data owner's requirements • Propose hardware and software changes to the system • Use change control process for implementing changes to ensure that data are protected during change • Ensure the security of the system • Generate metrics for the data owner to report
Subject matter experts	• Process understanding • Technical understanding of the computerized systems used in the process

- **Data stewards:** Responsible for enabling the requirements of the data owner for the system. (These people would typically be the power users or system administrators in the laboratory.)
- **Technology stewards:** Responsible for enabling the IT requirements of the data owner and a person or persons who, for a networked system, is the system owner or reports to the system owner. This role is essential for the segregation of duties and to avoid conflicts of interest when administering the system. Note that this role will not be found in a paper-based process because it is only used when a computerized system is involved.

The responsibilities of each role are listed in Table I and the interactions between these two roles and the data owner are shown in Figure 1. Subject matter experts, some of whom may be either data or technology stewards, are also mentioned in Table I and quality assurance input is only shown in Figure 1 but the responsibilities are many of those presented in Table II from Part I. To map from data governance roles to those currently used in laboratories, I have put titles in brackets in Table I—for example, a data steward is a laboratory administrator.

Looking at the three main roles above, you will find two of them are not mentioned in any data integrity guidance document: data steward and technology steward. The role of these stewards, and others, can be seen in the book by Plotkin (7). Why is there a need for data and technology stewards? The answer can be found in the discussion of who should be a process owner in *GAMP 5* (5) and outlined above. Typically, the data owner is the head or a section head of a laboratory, but often the work to be done in administering the system will be devolved to others such as super users or lab administrators and IT support staff if the system is connected to the network. This is the normal business process and these individuals are the data and technology stewards. Furthermore, because the data owner will specify the security, data quality, and data integrity requirements for the system, who better to ensure that they have been implemented than the second-person reviewers, another group of data stewards? You'll remember my comment earlier in this column about the need to integrate data integrity roles with normal business operations. Here is a very good example of that. Take the normal situation and simply reinforce or overlay the data integrity responsibilities on top.

Data Owner

It is important to realize that data integrity and data quality begin at the point of data acquisition by the process and not in the computer center. If data acquisition is compromised by poor working practices or by using an uncalibrated instrument, data integrity is compromised or lost from this point forward. Therefore, the data owner's responsibilities for a regulated computerized system from the business side include

- Defining what is required of a system in terms of data quality, data integrity, and data security. This process will result either in inputs to the configuration specification for the setting of application policies,

writing of standard operating procedures (SOPs) for using the system, or the agreement with IT to support the system (for example, backup, user account management, and so on). This step begins from the start of the analytical procedure.
- Assessment of the system to determine if there are vulnerabilities of the records contained therein. Although a system may be validated, record vulnerabilities may exist that have to be managed (8).
- Development of a remediation plan with the data and technology stewards for any remediation to secure the records and reduce or eliminate data vulnerabilities following the assessment.
- Approve access to the system for new users and changes in access privileges for existing ones for IT administrators to implement.
- Approval or rejection of change control requests.
- Approval for archiving data and removing them from the system.
- Receive feedback from the data stewards of the system of issues involving quality, integrity, and security of the spectroscopic data and implement any modifications of procedures for the data stewards to implement.

That's the good news for data owners.

Data Steward

The data stewardship concept is defined in the literature as the enabling capability of data governance. Defining different types of stewardship addressing different aspects of the data governance process is also described in the literature (7), but the focus in this column is only on data and technology stewards.

Because the data owner probably will not have the time or the training to implement the requirements for data integrity and quality that they have mandated, implementation is the role of the data stewards for the system:
- The data stewards, in the form of power users or super users, are the first point of contact for user questions for help with the system.
- The stewards will also be instrumental in ensuring the smooth running of the system with processes such as developing custom reports or custom calculations.
- As expert users of the system, they will be responsible for ensuring that the requirements for data integrity and data quality set by the data owner have been implemented and are working.
- They are also responsible for data queries and monitoring data integrity from a system perspective—for example, they are responsible for a regular review of system-level audit trails for system-related issues rather than data integrity problems or aiding quality assurance data integrity audits.

In monitoring the system from the business perspective, data stewards can raise issues for discussion with the data owner to resolve as noted earlier

Table II: The CMMI data maturity model (9)

Level	Description	Data Use
1. Performed	• Processes performed ad-hoc at project level • Processes not usually applied across business areas • Process discipline is primarily reactive e.g. corrective and not preventative actions • Improvements may exist but are not maintained or transferred within the organization	Data managed as a requirement for compliance with regulations
2. Managed	• Processes are planned and executed according to policy • Trained staff with adequate resources for producing controlled outputs • Relevant stakeholders involved • Processes are monitored, controlled and evaluated for adherence to the defined process	Awareness of the importance of managing data as an asset
3. Defined	• Standard process used consistently • Processes for specific needs modified from standard processes to meet organisation's guidelines	Data treated at organizational level as critical for successful mission performance
4. Measured	• Process metrics defined and used for data management • Management of variance, predication and analysis • Process performance managed across the life of the process	Data are treated as a source of competitive advantage
5. Optimized	• Process performance is optimized by applying Level 4 analysis to target process improvement opportunities • Best practices shared with peers and industry	Data are seen as critical for survival in a dynamic and competitive market

in this section.

Is a Lab Administrator a Data Steward?

Although data stewards are involved with data governance outside of the pharmaceutical industry, we need to see how this role can be overlaid onto the situation in a regulated laboratory. For most systems, either stand-alone or networked, the data owner may not be involved in some of the technical administration of the application such as the generation of spectral libraries, creation of custom reports, and custom calculations or macros. Technical administration is the role of the laboratory administrators. You can see that adding the responsibilities involved for data stewardship in Table I would be a logical step within an overall data governance framework and to integrate governance within the current roles typically used in a laboratory.

Is a Technology Steward a System Owner?

Recall the definition of system owner from *Annex 11* as the person who is responsible for the availability and maintenance of a computerized system and for the security of the data residing on that system. This role, in my view, should be performed by the IT department. In particular, the system owner could be the head of the functional IT group responsible for system support. An alternative approach is that the system owner could be in the laboratory or business, but that would only work with larger organizations that have the capacity for the headcount. In smaller organizations, the role of system owner would need to be delegated directly to the IT department under an agreement with the process or data owner.

For a networked application, technology stewards are members of the IT department who would be responsible for the administration of a networked application, logical security, backup or recovery, and other support functions and carry out the responsibilities outlined in Table I. However, if the spectroscopy system is stand-alone and has few users, then the data owner is also the data steward and the technology steward. Three hats and no pay rise.

Segregation of Duties

In this data governance framework, it is important that there is a segregation of duties. For example, there needs to be separation of administrator functions for configuration of the application from the normal analytical users of the system. In addition, access to data files in operating system directories, the system clock and the recycle bin needs to be restricted for laboratory users.

The Short Straw . . .

Look around any regulated laboratory and you will see a data integrity disaster in operation. There are your lovely toys—sorry, spectrometers—that are operated by a software operating on a stand-alone workstation. Do you want the good news or the bad news? Good news? OK, there is none! The bad news comes in a variety of forms:

- You, the data owner, are now also the system owner because the computer is not connected to the network—you are now doing user account management, documenting the configuration of the software, and backing up the data, and this is a conflict of interest.
- It is highly likely that you are using the system as a hybrid by generating electronic records and signing paper printouts.
- Most of your electronic records are stored in directories within the operating system that any user can access by going outside of the operating system and deleting files. Moreover, such users can also access the system clock, which may not be checked; they can also access the recycle bin.

Life is wonderful, if you don't think about the problems with your software

and the electronic records. How do we resolve this situation?

Defining Data Integrity and Security of a System

You may remember from Table I in Part I that the focus was on the access to data and hence the records generated, interpreted, and reported by it. Therefore, you as the data or process owner are responsible for assessing the processes and systems for which you are responsible for the vulnerability of the records over the lifetime of the data. This assessment will be coordinated by the corporate data governance steering committee or their local equivalent.

The aim of this assessment is to identify the vulnerabilities of the records and remediate in two ways:

- Short-term remediation: This process involves quick fixes to ensure that records are protected, such as implementing operating system security to prevent access to the records, the system clock, and the recycle bin. Electronic records with associated metadata should be transferred to the network and be backed up by the IT department. Adding a network card to the workstation should enable the data to be backed up to secure network storage.
- Long-term remediation: This process ensures that the system and the process it automates acquires and manages data to ensure quality, reliability, and integrity of the records. Let's explore this area briefly now.

The Hybrid System Nightmare

A hybrid system is the worst possible situation because the data owner has to ensure that the electronic records created by the software are linked to the signed paper printouts. Managing and coordinating two disparate media forms over the lifetime of the data is difficult. However, don't just take my word for it, look at what the WHO data integrity guidance (4) says:

- "Data integrity risks are likely to occur and to be highest when data processes or specific data process steps are . . . hybrid, . . .
- "The use of hybrid systems is discouraged . . .
- "The hybrid approach is likely to be more burdensome than a fully-electronic approach; . . .
- "Replacement of hybrid systems should be a priority.
- "In the hybrid approach, which is not the preferred approach, paper printouts of original electronic records . . ."

Are you getting the message?

While the aim of short term remediation is to ensure that the record vulnerabilities are reduced to acceptable levels, longer-term replacement of these systems is essential. Again, the aim here is to provide substantial business benefit to the laboratory with the remediation and not just to replace one hybrid system with another as was the case with Part 11 remediation. Automation of a laboratory process must have the aim of improving working practices, speeding up work, and ensuring data integrity. However, if the new laboratory process fails to eliminate the majority of paper records or the way the software works is not managed correctly then all that happens is that the process becomes an automated mess and data integrity cannot be ensured. Back to square one.

The problem is that the majority of spectroscopic systems are very poorly designed. Examples include:

- systems designed to work as a hybrid with no electronic signatures;
- electronic signatures implemented improperly in that the signature is not applied to the record but recorded only as an audit trail entry;
- a system operated as a stand-alone system with no option to work as a networked system that would allow users to review data at a second workstation;
- a system in which data are acquired to a single hard drive and not to a secure network drive;
- a system in which data are managed in directories in the operating system rather than in a database; and
- poor audit trail review functions that highlight if good manufacturing practice (GMP) critical data have been modified or deleted.

Unfortunately, users have not pressured suppliers to ensure that the software is adequate to meet changing regulatory requirements and suppliers only react to market forces.

Data Maturity Model

You will recall in Part 1 of this column, I stated that the primary reason for data governance should be for business rather than regulatory reasons. Again, we step outside of

the confines of the regulated world and bring in a wider perspective from the CMMI Institute. Carnegie-Mellon University of Pittsburgh (CMU) has the Software Engineering Institute (SEI) as one of its faculties. The SEI has designed the capability maturity model (CMM) to classify an organization's software development ability into one of five categories. A further refinement of this model is CMMI for implementation of software within organizations and has given rise to the CMMI Institute. A data maturity model (DMM) has been developed (9). The DMM is a five category model that describes an organization's maturity for dealing with data and an edited version of this is shown in Table II.

As can be seen in Table II, DMM Level 1 is essentially ad hoc management of data, which in a pharmaceutical context is producing and managing data because the regulations say you must. As we go up toward DMM Level 5 there is increasing emphasis on the design of processes that generate and use data effectively as well as a realization that data are a strategic asset and must be managed as such (9). Hence the need for effective data governance from the boardroom down in an organization. At the higher levels, metrics are collected and analyzed not just for monitoring the effectiveness of a data generating process but also to improve it.

One of the aims of data governance should not be a way to keep the regulators happy, but to ensure the survival and growth of organizations that need the integrity of their records assured.

Don't Forget Paper Records!

Although the focus in this column has been on electronic records, data governance and data integrity also needs to consider paper records that are created and used in analysis. Chris Burgess and I wrote a recent paper on the control of blank forms (10) to address the regulatory concerns in the WHO, FDA, EMA, and PIC/S guidance documents (4,11–13). Blank forms are not the end of the paper trail—don't forget balance printouts, laboratory notebooks, equipment logs, and so forth,

Summary

In this two-part column series, we have looked at data governance from the board room to the laboratory bench for a regulated organization. We have discussed the organizational structures, roles, and responsibilities for ensuring data integrity. In the laboratory, data ownership and data stewards are important for ensuring the integrity of data acquired, processed, and reported is complete, consistent, and accurate. However, don't forget that this column series has focused on computerized systems because we are looking at spectroscopic analysis. There are manual paper-based processes in many laboratories that also have to be analyzed for risk to the records generated and used. As a parting thought, all data governance for data integrity must be integrated into the pharmaceutical quality system for an organization.

Acknowledgments

I would like to thank Mark Newton, Kevin Roberson, Lorrie Schuessler, and Yves Samson for their helpful review comments made in preparation of the two parts of this column.

References

(1) R.D. McDowall, *Spectroscopy* **32**(2), 32–38 (2017).
(2) J. Avellanet and E. Hitchens, *Considerations for a Corporate Data Integrity Program* (International Society of Pharmaceutical Engineering, Tampa, Florida, 2016).
(3) Medicines and Healthcare Products Regulatory Agency, *GMP Data Integrity Definitions and Guidance for Industry,* 2nd Edition (MHRA, London, England, 2015).
(4) World Health Organization, *WHO Technical Report Series No.996 Annex 5 Guidance on Good Data and Records Management Practices* (WHO, Geneva, Switzerland, 2016).
(5) ISPE, *Good Automated Manufacturing Practice (GAMP) Guide Version 5* (International Society for Pharmaceutical Engineering, Tampa, Florida, 2008).
(6) European Commission Health and Cosumers Directorate-General, *EudraLex - Volume 4 Good Manufacturing Practice (GMP) Guidelines, Annex 11 Computerised Systems* (European Commission, Brussels, 2011).
(7) D. Plotkin, *Data Stewardship. An Actionable Guide to Effective Data Management and Data Governance* (Morgan Kaufman, Waltham, Massachusetts, 2014).
(8) R.D. McDowall, *LCGC Europe* **30**(1), 93–96 (2016).
(9) Data Management Maturity (DMM) Model (CMMI Institute, Pittsburgh, Pennsylvania, 2014).
(10) C. Burgess and R.D. McDowall, *LCGC Europe* **29**(9), 498–504 (2016).
(11) Pharmaceutical Inspection Co-operation Scheme, *PIC/S PI-041 Draft Good Practices for Data Management and Integrity in Regulated GMP/GDP Environments* (PIC/S, Geneva, Switzerland, 2016).
(12) European Medicines Agency, *EMA Questions and Answers: Good Manufacturing Practice: Data Integrity* (EMA, 2016, available from: http://www.ema.europa.eu/ema/index.jsp?curl=pages/regulation/general/gmp_q_a.jsp&mid=WC0b01ac058006e06c#section9).
(13) US Food and Drug Administration, *Draft Guidance for Industry Data Integrity and Compliance with cGMP* (FDA, Silver Spring, Maryland, 2016).

R.D. McDowall is the Principal of McDowall Consulting and the director of R.D. McDowall Limited, as well as the editor of the "Questions of Quality" column for *LCGC Europe*, *Spectroscopy*'s sister magazine. Direct correspondence to: SpectroscopyEdit@UBM.com

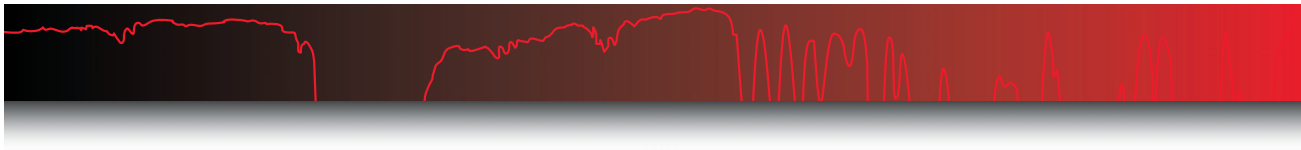

IR Spectral Interpretation Workshop

Alcohols—The Rest of the Story

Our survey of the spectroscopy of the C-O bond continues where we complete our discussion of alcohols and discuss how to distinguish pure alcohols, alcohol–water mixtures, and pure water from each other.

Brian C. Smith

In the last column (1) I introduced you to the spectroscopy of the C-O bond, and we covered how to interpret the spectra of primary alcohols. As I discussed then, in addition to primary alcohols, secondary alcohols, tertiary alcohols, and phenols can be analyzed by infrared spectroscopy as well. The chemical structures of primary, secondary, and tertiary alcohols are shown in Figure 1.

Remember that in general alcohols have a broad, strong O-H stretch at 3350 ± 50 cm^{-1} (assume all peak positions stated after this are in cm^{-1} units), an in-plane –OH bend at 1350 ± 50, and an O-H wag at 650 ± 50 (1). Lastly, primary alcohols typically have a C-C-O asymmetric stretch (hereinafter called the C-O stretch) between 1000 and 1075. As we will learn in this installment, the key to distinguishing these alcohols from each other is the position of the C-O stretching peak.

The Spectra of Secondary and Tertiary Alcohols

A spectrum of a secondary alcohol, called isopropyl or "rubbing" alcohol, is shown in Figure 2, and its peak assignments are shown in Table I. As we have learned (1), the infrared peaks of alcohols are broadened because of hydrogen bending and are hence easy to spot. In Figure 2 the OH stretch is labeled A at 3349, the in-plane bend labeled C appears at 1309, and the -OH wag labeled G appears at 655. Recall that the C-O stretch is frequently the largest peak between 1300 and 1000 (1). Following this rule we can assign the peak labeled D at 1129 as the C-O stretch of isopropyl alcohol. Note that this is higher in wavenumber than the range quoted for primary alcohols of 1075 to 1000. For secondary alcohols generally the C-O stretch falls between 1150 and 1075. Thus, a C-O stretch below 1075 can be assigned as a primary alcohol, and a C-O stretch above 1075 can be assigned as a secondary alcohol. The C-C-O symmetric stretch of isopropyl alcohol is at 817 and is labled F in Figure 2. Peak B is a "split" umbrella mode due to the branch point in isopropyl alcohol. More on this type of peak and branch points in a future column. Peak E is from a C-C stretching vibration. Carbon-carbon stretching vibration peaks are typically not this intense. However, the oxygen attached to the carbon atoms polarizes these bonds, increasing the change in dipole moment with respect to distance during the vibration, resulting in an increase in peak intensity.

The spectrum of a tertiary alcohol, *tert*-butanol, is seen in Figure 3. The OH peaks fall as expected, with the stretch at 3371, the in-plane bend at 1366, and wag at 648. Note that *tert*-butanol also has a split umbrella mode with peaks at 1379 and 1366 because of its branch point. The reasonably intense peak at 914 is the symmetric C-C-O stretch. The biggest peak between 1300 and 1000 is at 1202 and is assigned as the C-O stretch. In general for tertiary alcohols this peak falls between 1210 and 1100. Unfortunately, this range overlaps significantly with the

range for secondary alcohols. Using the C-O stretching peak position as noted in Table II, primary and secondary alcohols can be distinguished, primary and tertiary alcohols can be distinguished, but secondary and tertiary alcohols may or may not be distinguished depending upon where their C-O stretches fall. Unfortunately, there are no other useful IR peaks to solve this problem. Other information, such as a ^{13}C nuclear magnetic resonance (NMR) spectrum, may be needed to distinguish secondary and tertiary alcohols from each other.

The Solution to Last Column's Interpretation Problem, and This Month's Problem

Working our way from left to right across the spectrum in Figure *i*, the first peak encountered is a strong and broad one at 3342, strongly indicating the presence of an OH bond in the sample. The broad OH wag at 660 confirms that this molecule is an alcohol. To identify the type of alcohol we look for the biggest peak between 1300 and 1000, which is at 1058 confirming this is a primary alcohol whose skeletal framework is R-CH_2-OH.

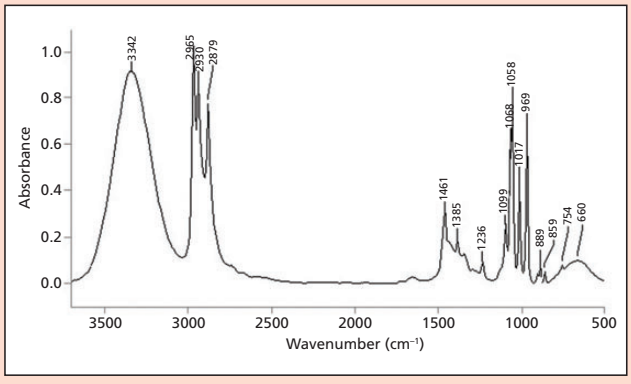

Figure *i*: The infrared spectrum of propyl alcohol, C_3H_8O, the solution to last column's interpretation problem.

Table *i*: The peak assignments for propyl alcohol.

Peak	Assignment
3342	O-H stretch
2965	CH_3 asymmetric stretch
2938	CH_2 asymmetric stretch
2879	CH_3 asymmetric stretch
1385	CH_3 umbrella mode
1058	Primary alcohol C-O stretch
889	C-CH_2-O symmetric stretch
660	O-H out-of-plane bend

$CH_3CH_2CH_2$-OH

Figure *ii*: The chemical structure of propyl alcohol, the solution to last column's interpretation problem.

Coming back to the C-H stretches, note that there are none above 3000 but that there are three between 2850 and 3000. The position of these peaks confirms that all carbons present are saturated, and the fact that there are three of them indicates there are CH_2 and CH_3 groups present (2). The presence of a methyl group umbrella mode at 1385 confirms the presence of the methyl group, and the absence of any peaks at 720 ± 10 means that the alkyl chains present have less than four CH_2 groups in a row (2).

The final thing to do here is determine the CH_2/CH_3 ratio. Because by definition primary alcohols have at least one methylene group, and we know that there is a CH_3 present, the CH_2/CH_3 ratio could be 1. The only primary alcohol that meets this description is ethyl alcohol, whose spectrum we have seen previously (1), and it does not look like the problem spectrum (besides, I would never assign you a spectrum as a problem that you have previously seen!). Since the alkyl chain must have fewer than four methylenes in a row, the only other possibilities are chains with two or three CH_2 groups. In the primary alcohol class this narrows us down to propyl alcohol or butyl alcohol. I am afraid this is far as we can push the analysis using just this spectrum, consulting a spectral atlas or a library search would resolve the problem. As we have seen before it is not always possible to get exact alkyl chain length from an infrared spectrum by itself. It turns out the CH_2/CH_3 ratio is 2, and the sample is propyl alcohol (propanol), whose structure is shown in Figure *ii* and whose peak assignments are shown in Table *i*.

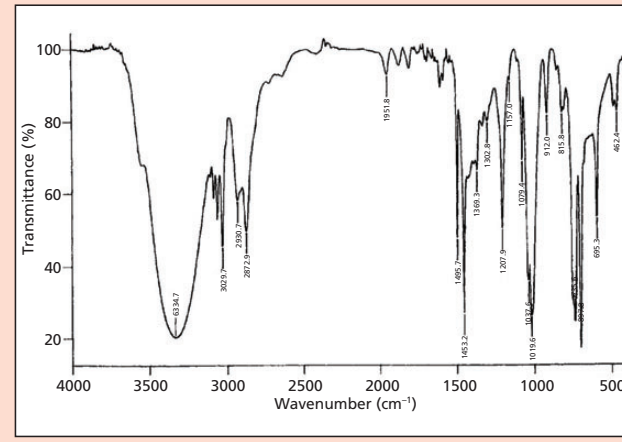

Figure *iii*: The infrared spectrum of a liquid measured as a capillary thin film (hint: to make your life easier, assume the peak at 2872 is at 2855).

In a previous column I discussed how to use the intensity ratio of the methyl and methylene asymmetric C-H stretches to estimate CH_2/CH_3 ratio (3). I did not do that for this problem because the way the spectrum was plotted it is difficult to tell where the peaks end and the peak markings begin, making it impossible to use this approach in this particular example. I apologize for the inconvenience.

Next Interpretation Problem

Our next interpretation problem is shown in Figure *iii*. Here's a hint: To make your life easier, assume the peak at 2872 is at 2855.

Table I: Peak assignments for the infrared spectrum of isopropyl alcohol		
A	3349	O-H stretch
B	1379, 1369	Split CH_3 umbrella mode
C	1309	O-H in-plane bend
D	1129	C-C-O asymmetric stretch
E	952	CH_3-C- CH_3 stretch
F	817	C-C-O symmetric stretch
G	655	O-H out-of-plane bend

Phenols

As stated in the last column (1), phenols contain an OH group attached to an aromatic ring. The spectrum of the namesake molecule of this class, phenol, is shown in Figure 4.

This spectrum is one of the busiest we have seen so far, and I included it not to confuse you, but to be real. As the molecules we study include more and more functional groups, their spectra will become more complicated and unfortunately more challenging to interpret. Consider studying this spectrum good preparation for what is to come in future columns.

The OH stretch at 3345 and in-plane bend at 1367 can be easily seen in Figure 4. This latter peak is in the same wavenumber range as methyl group umbrella modes; however, note that there are no methyl C-H stretches below 3000, and the 1367 peak is too broad to be from a CH_3 group. The largest peak between 1300 and 1000 is at 1231, and is assigned as the C-O stretch. In general, for phenols this peak falls between 1260 and 1200. Usually phenols can be distinguished from primary and secondary alcohols based on the position of their C-O stretch, and can often be distinguished from tertiary alcohols unless the C-O stretch falls from 1210 to 1200. In Figure 4 this is the case, but we know this is not a saturated alcohol because of the lack of C-H stretches between 3000 and 2800.

We would expect the spectrum of phenol to have an OH wag at 650 ± 50, but it is not obvious on an initial examination of Figure 4. However, if you look closely there is a broad envelope in this region with sharper benzene ring peaks on top of it. So the wag is there—it's just hard to assign a peak position to it. This is often a problem for phenols, so be on the lookout for broad envelopes like this one at low wavenumber if you suspect a phenol is present in a sample.

Table II summarizes the peak positions for the various alcohols.

Distinguishing Alcohols from Water

The infrared spectrum of liquid water is shown in Figure 5. Both water and alcohols have an OH bond and thus have OH stretching peaks that are intense, broad, and fall in the same place around 3300. Because of this shared spectral feature,

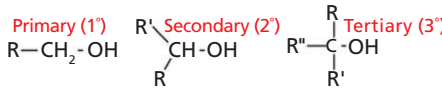

Figure 1: The structures of primary, secondary, and tertiary alcohols. The R-groups represent non-hydrogen atoms, typically carbons.

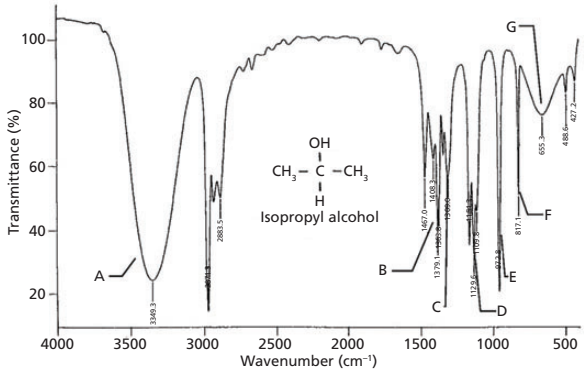

Figure 2: The infrared spectrum of isopropyl alcohol, C_3H_8O, measured as a capillary thin film.

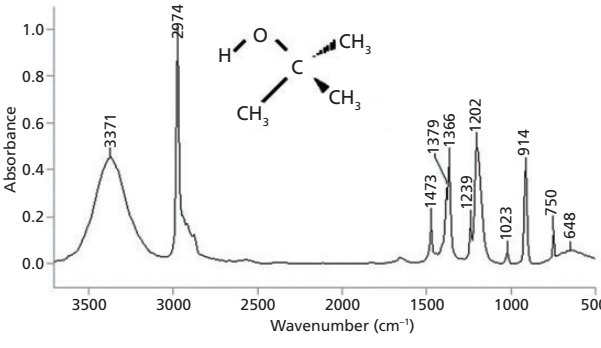

Figure 3: The infrared spectrum of *tert*-butanol, $C_4H_{10}O$, measured as a capillary thin film.

the presence of an OH stretch in a spectrum is not diagnostic for the presence of an alcohol, only for the presence of an OH group. If you see an OH stretch then how can you distinguish the spectra of a pure alcohol, water, or a mixture of the two? The solution to this problem is Table III.

Note in Figure 5 that water has a scissors bending peak near 1630. This peak occurs because in water the oxygen has two hydrogens attached to it. By definition alcohols only have one O-H bond, and hence their spectra will not exhibit this peak. Also remember that water is inorganic and does not have a C-O bond, thus it will not have the C-O stretching peak that the spectra of all alcohols exhibit. This is the information that was used to construct Table III, where the presence or absence of these peaks can be used to distinguish these three types of samples from each other. For example, pure water has an OH stretch and a scissors peak, but no C-O stretch. A pure alcohol has an OH stretch and no scissors peak, but does have a C-O stretching peak. Lastly, a mixture of an alcohol and water has an OH stretch, a scissors peak from the water present, and a C–O stretch because of the alcohol present. Water–alcohol mixtures are relatively common because some alcohols are hygroscopic and are readily soluble in water. A mnemonic for remembering Table III is that for pure water the pattern is yes yes no, for pure alcohols it is yes no yes, and for a mixture of the two it is yes yes yes. This table should allow you to distinguish these types of samples from each other.

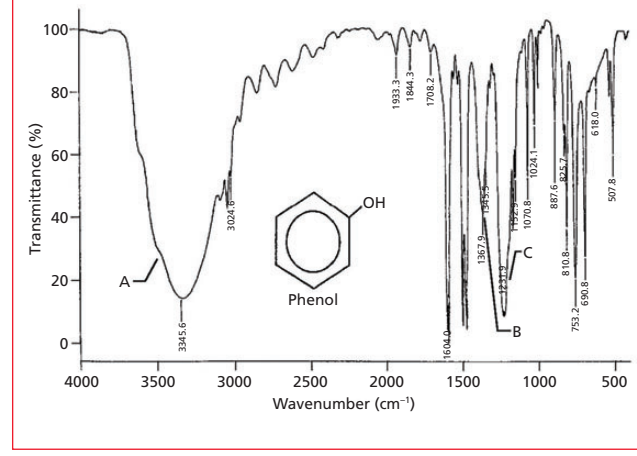

Figure 4: The infrared spectrum of phenol, C_6H_6O, measured as a capillary thin film.

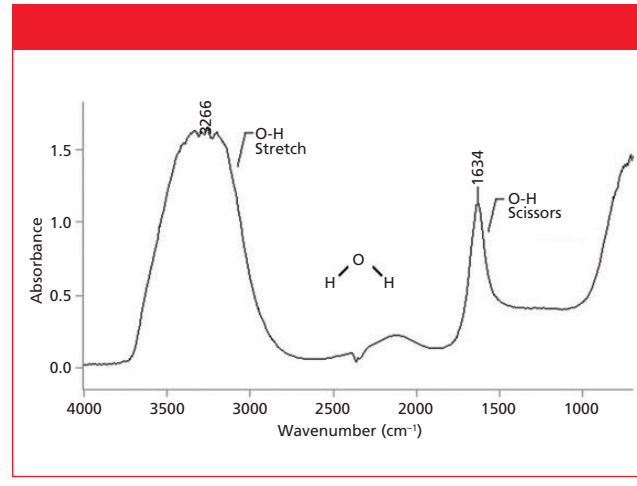

Figure 5: The infrared spectrum of liquid water.

Table II: The diagnostic infrared peak positions for alcohols

Substitution Pattern	C-O Stretch	O-H Stretch	O-H Bends
All	—	3350 ± 50	1350 ± 50, 650 ± 50
Primary	1075–1000	3350 ± 50	1350 ± 50, 650 ± 50
Secondary	1150–1075	3350 ± 50	1350 ± 50, 650 ± 50
Tertiary	1210–1100	3350 ± 50	1350 ± 50, 650 ± 50
Phenols	1260–1200	3350 ± 50	1350 ± 50, 650 ± 50

Table III: How to distinguish pure alcohols from water or a mixture of the two

Sample Contains	O-H Stretch ~3400	O-H Scissors ~1630	C-O Stretch 1300–1000
Water	Yes	Yes	No
Alcohol	Yes	No	Yes
Both	Yes	Yes	Yes

Summary

The spectra of alcohols and phenols typically exhibit a large peak between 1300 and 1000 that can be assigned as the asymmetric C-C-O stretch ("C-O stretch"). For primary alcohols this peak falls from 1075 to 1000, for secondary alcohols from 1150 to 1075, for tertiary alcohols from 1210 to 1100, and for phenols from 1260 to 1200. Thus the peak range for primary alcohols is unique and they are easily distinguished from all other secondary alcohols can be distinguished from primary alcohols but their C-O stretching has some overlap with tertiary alcohols, and phenols can usually be distinguished unless their C-O stretching peak falls between 1210 and 1200. Information about alcohol C-O stretching peak positions is summarized in Table II. The spectra of water, pure alcohols, and their mixtures can be distinguished using the presence or absence of the water scissors peak at 1630 and the alcohol C-O stretch between 1300 and 1000, as detailed in Table II.

References

(1) B.C. Smith, *Spectroscopy* **32**(1), 14–21 (2017).

(2) B.C. Smith, *Spectroscopy* **30**(7), 26–31 (2015).

(3) B.C. Smith, *Spectroscopy* **30**(9), 40–45 (2015).

Brian C. Smith, PhD, is the West Coast Business Development Manager for CAMO Software, a company that sells chemometric, multivariate analysis, and process control software. Before joining CAMO, Dr. Smith ran his own FT-IR training and consulting business for more than 20 years. Dr. Smith has written three books on infrared spectroscopy: *Fundamentals of FTIR* and *Infrared Spectral Interpretation*, both published by CRC Press, and *Quantitative Spectroscopy: Theory and Practice* published by Academic Press. He can be reached at: SpectroscopyEdit@UBM.com

For more information on this topic, please visit our homepage at: www.spectroscopyonline.com

Pump–Probe Microscopy: Theory, Instrumentation, and Applications

Excited-state dynamics provides an intrinsic molecular contrast of samples examined. These dynamics can be monitored by pump–probe spectroscopy, which measures the change in transmission of a probe beam induced by a pump beam. With superior detection sensitivity, chemical specificity, and spatial–temporal resolution, pump–probe microscopy is an emerging tool for functional imaging of nonfluorescent chromophores and nanomaterials. This article reviews the basic principles, instrumentation strategy, data analysis methods, and applications of pump–probe microscopy. A brief outlook is provided.

Pu-Ting Dong and Ji-Xin Cheng

As a pioneer of femtochemistry, Nobel laureate Ahmed Hassan Zewail (1–3) recorded the snapshots of chemical reactions with sub-angstrom resolution through an ultrafast femtosecond transient absorption (TA) technique. In a transient absorption experiment, a laser pulse pumps a molecule into an excited state. The excited state itself exhibits relaxation dynamics on the femtosecond or picosecond timescale. A second laser pulse then probes the population in the excited state at different temporal delays with respect to the excitation. This analysis method reveals the dynamics of the excited state and is termed as *pump–probe spectroscopy*.

Pump–probe microscopy, also known as *transient absorption microscopy*, is an emerging nonlinear optical imaging technique that probes the excited state dynamics, which is related to the third-order nonlinearity (3,4). Pump–probe microscopy is an attractive spectroscopic imaging technique with the following advantages: First, it is nondestructive to cells and tissues and can be performed without tissue removal (5). Thus, it can be used as a repeatable diagnostic tool. Second, it is a label-free technique and doesn't need an exogenous target (4). Third, as a nonlinear optical technique, pump–probe microscopy can image endogenous pigments with three dimensional (3-D) spatial resolution (6). Fourth, unlike linear absorption, which suffers from scattering in a tissue sample, the pump–probe technique only measures absorption at the focal plane, which offers optical sectioning capability (6). Fifth, compared to scattering measurements, this absorption-based method has a weaker dependence on the particle and thus is highly sensitive to nanoscale subjects (8–11). Sixth, pump–probe microscopy with near-infrared laser pulses permits biological applications with an enhanced penetration depth and a lower level of tissue damage (12).

In 1990s, Dong and coworkers used pump–probe microscopy to measure fluorescence lifetime (13). In 2007, the Warren group reported pump–probe imaging with a high-frequency modulation scheme (14). Their work demonstrated the feasibility of imaging melanin by using two-color two-photon absorption (TPA) or excited state absorption (ESA) processes. Since then, extensive research has been conducted by harnessing the merits of pump–probe microscopy. A majority of the research focused on nonfluorescent chromophores such as hemoglobin and cytochromes, which absorb light but do not emit fluorescence efficiently (15). Fu and colleagues used two-color absorption to measure the degree of oxygenation based on the different decay constants of deoxyhemoglobin and oxyhemoglobin (16). Pump–probe microscopy can efficiently discern hemoglobin and melanin, the two major absorbers in a biological tissue. Based on their signatures from the time-resolved curves, hemoglobin shows a purely positive response because of

excited state absorption, whereas melanin (eumelanin and pheomelanin) demonstrate a negative (ground state bleaching) signal when the pump beam and probe beam spatially and temporally overlap (5). In addition, pump–probe microscopy enables the discrimination of melanomas by determining the ratio between eumelanin and pheomelanin. Melanin play an important role in skin and hair pigmentation and melanomas (17). Without external staining, pump–probe imaging yielded novel insight into the differentiation of eumelanin and pheomelanin among thin biopsy slices and has been used to probe the metastatic potential of melanocytic cutaneous melanomas (16). Besides applications to pigments in biological tissue, pump–probe microscopy has also been applied to distinguish various kinds of pigments in arts based on their decay differences (18–21).

Another significant application of pump–probe microscopy is for characterization of single nanostructures including gold nanorods (22) and single-wall nanotubes (SWNTs) (23–26). Specifically, Jung and coworkers for the first time deployed the phase of the pump–probe signal as a contrast to distinguish semiconducting carbon nanotubes from metallic ones (25). Tong and colleagues further used this contrast for imaging semiconducting and metallic nanotubes in living cells (26). By tuning the excitation wavelength, which is resonant with the lowest electronic transition in SWNTs, Huang and colleagues exploited the band-edge relaxation dynamics in isolated and bundled SWNTs (23). Through assembling SWNTs with CdS, Robel and colleagues demonstrated the charge-transfer interaction between photoexcited CdS nanoparticles and SWNTs by transient absorption (24).

In this review, we summarize the contrast mechanisms and instrumentation strategies of pump–probe microscopy and highlight some of these significant applications. Because of space limitations, we could not cover the entire literature and would recommend to the readers other excellent articles in this field (27–32).

Pump–Probe Theory

In a typical pump–probe measurement, the pump-induced intensity change of the probe is measured by a lock-in amplifier referenced to the modulated pump pulse. Then this change is normalized by the probe beam intensity to generate $\Delta I_{pr}/I_{pr}$ (33). To express this process at molecular level, we define the absorption coefficient for an electronic transition between level "i" and level "j" as

$$\alpha_{ij}(\omega) = \sigma_{ij}(\omega)\,(N_i - N_j) \qquad [1]$$

where $\sigma_{ij}(\omega)$ is the cross section from electronic state i to j, and N_i and N_j are the populations of the initial and final states, respectively. Conventionally, α is positive for absorption and negative for gain (33).

The pump pulse acts on the sample by changing the energy level population, $N \rightarrow N + \Delta N$. As a consequence,

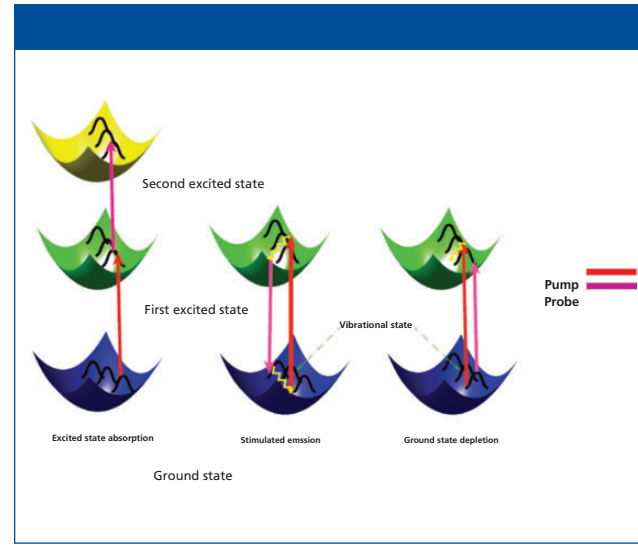

Figure 1: Three major processes in a pump–probe experiment: (a) Excited state absorption, (b) stimulated emission, and (c) ground-state depletion. For ground-state depletion, the number of the molecules in the ground state is decreased upon photoexcitation, consequently increasing the transmission of the probe pulse. For stimulated emission, photons in its excited state can be stimulated down to the ground state by an incident light field, thus leading to an increase of transmitted light intensity on the detector. In the case of excited-state absorption, the probe photons are absorbed by the excited molecules, promoting them to the higher energy levels.

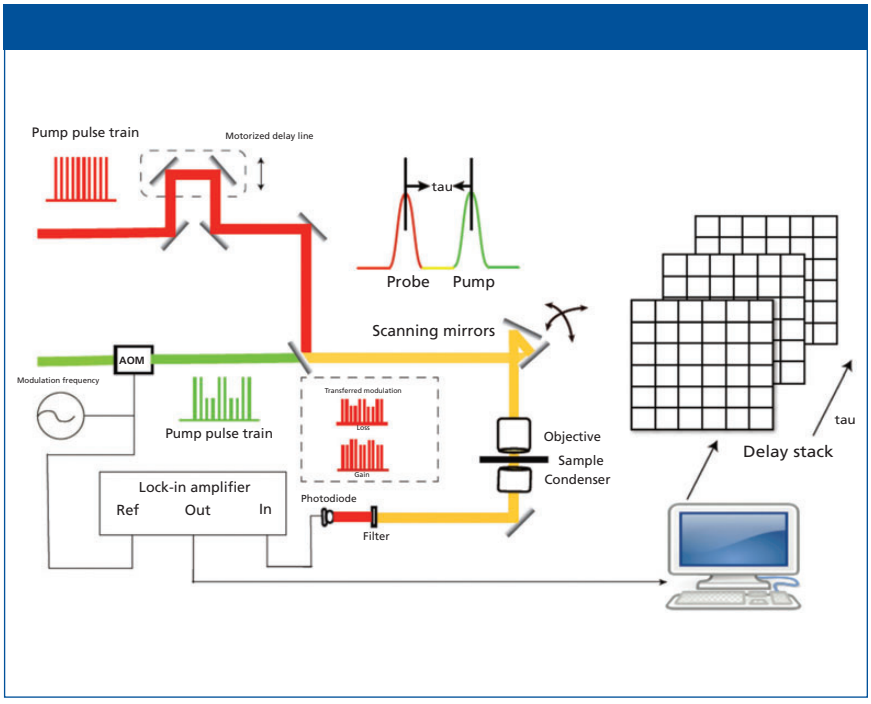

Figure 2: Schematic illustration of pump–probe microscopy.

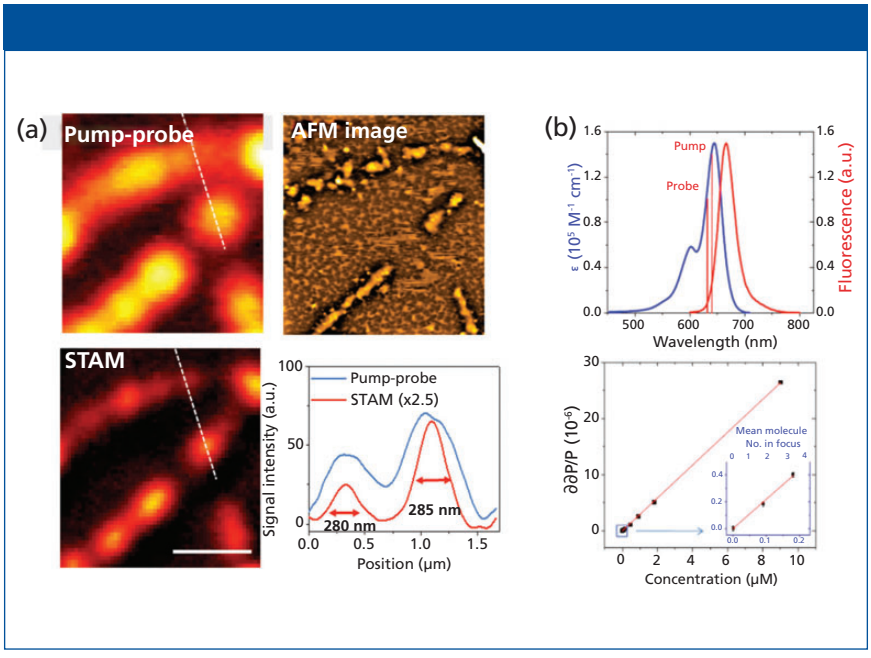

Figure 3: Pump–probe microscopy with subdiffraction spatial resolution and single-molecule detection sensitivity. (a) Subdiffraction-limited imaging of graphite nanoplatelets. Image from conventional transient absorption microscopy (top left) and AFM image of graphite nanoplatelets (top right). Image from saturation transient absorption microscopy (bottom left) and intensity profiles along the lines indicated by the dashed lines in pump–probe image and STAM image (bottom right). Adapted with permission from reference 47. (b) Ground-state depletion microscopy with detection sensitivity of single-molecule at room temperature. Ensemble absorption and emission spectra of Atto647N in pH = 7 aqueous solution (top). The wavelengths of pump and probe beams are indicated. Ground-state depletion signal as a function of concentration of aqueous Atto647N solution (bottom). The power is 350 μW for each beam. The blue frame shows the points at lowest concentrations, indicating single-molecule sensitivity is reachable. Figures adapted with permission from reference 40.

the population of excited states will increase at the expense of that of the ground state. Such change is measured by the probe beam:

$$\frac{\Delta I_{pr}}{I_{pr}} = -\sum_{i,j}\alpha_{ij}(\omega)\Delta N_j d \qquad [2]$$

where d is the sample thickness. The expression is derived from the Lambert-Beer relation within the small signal approximation. The "j" term describes all possible excited states (33).

Depending on the probe energy, three effects on the transmitted pulse can be observed: When the probe pulse is resonant with $i \rightarrow j$ transitions ($i \neq 0$), then the probe pulse is absorbed by the molecule, reducing the transmission of the probe pulse. This negative $\Delta I_{pr}/I_{pr}$ signal change is therefore called excited state absorption (ESA). When the probe pulse is resonant with $0 \rightarrow j$ transmission, the probe transmission is enhanced upon pump excitation. This positive $\Delta I_{pr}/I_{pr}$ phenomenon is called ground-state depletion (GSD). When the lowest excited state is dipole-coupled to the ground state and the probe pulse is resonant with the transition, stimulated emission (SE) occurs. An increased transmission is observed in a SE process.

These three major processes are illustrated in Figure 1. A detailed description is provided in the following sections.

Excited-State Absorption

Excited-state absorption (ESA) is a process where the probe photons are attenuated by excited states as shown in Figure 1. Since the 1970s, picosecond laser–based ESA measurements have been extensively used to measure ground and excited-state dynamics (34,35). Compared to two-photon absorption, which goes through a virtual intermediate state, excited-state absorption significantly enhances the detection sensitivity by bringing a resonance with a real intermediate electronic state. The mechanism for this process (36) can be described using the following equation:

$$\Delta I_{pr} = -\int \frac{N_0 \sigma_{pu}[\sigma'_{pr} - \sigma_{pr}] I_{pu} I_{pr} \exp\left(-\frac{\Delta t}{\tau}\right)}{\hbar \nu_{pv}} dz \quad [3]$$

where N_0 is the molecular concentration at ground state; σ_{pr} and σ'_{pr} are the linear absorption cross sections of the ground state and excited states for the probe beam, respectively; ν_{pu} represents the pump frequency and τ is the lifetime of the excited state (assume this is a single-exponential decay); and Δt is the time delay between pump beam and probe beam. I_{pu} and I_{pr} denote the intensity of pump beam and probe beam, respectively. In the presence of a pump pulse, excited-state population would give birth to the transmission changes of the probe. Equation 3 demonstrates that only at $\Delta t = 0$ when the pump beam and probe beam are spatially and temporally overlaid can ΔI_{pr} have the biggest value. As Δt becomes longer, ΔI_{pr} depicts as an exponential decay curve convoluted with an instrumental response function that is a Gaussian function.

Stimulated Emission

When interrogating the short-lived excited states in pump–probe experiments, the photons in the excited states are stimulated down to the ground state by a time-delayed probe pulse as shown in Figure 1. This process is called *stimulated emission* (37). The absorption coefficient decreases with increasing excitation irradiance. The decrease in absorption happens due to the annihilation of the number densities of both the ground state and the state being excited, this process can be portrayed as equation 4:

$$\Delta I_{pr} = -\int \frac{N_0 \sigma_{pu} \sigma_{pr} I_{pu} I_{pr} \exp\left(-\frac{\Delta t}{\tau}\right)}{\hbar \nu_{pv}} dz \quad [4]$$

From equation (4), we can tell at $\Delta t = 0$, strongest signal is achieved. As Δt becomes longer, the transmission change of probe also demonstrates an exponential decay curve convoluted with Gaussian function. Based on the stimulated emission, Min and colleagues achieved nanomolar detection sensitivity of nonfluorescent chromophores (37). The integrated intensity attenuation of the excitation beam can also be expressed as

$$\frac{\Delta I_{pu}}{I_{pu}} = -\frac{N_0 \sigma_{01}}{S} \sim 10^{-7} \quad [5]$$

where $S \sim 10^{-9}$ cm^2 denotes the beam waist, and $\sigma_{01} \sim 10^{-16}$ cm^2 represents the absorption cross section from ground state to the first electronic state. The stimulation beam will experience a transmission gain after interaction with the molecules:

$$\frac{\Delta I_{pr}}{I_{pr}} = -\frac{N_0 \sigma_{10}}{S} \sim 10^{-7} \quad [6]$$

$$\Delta I_{pr} \propto \frac{N_0 I_{pu} I_{pr} \sigma_{10} \sigma_1}{S^2} \quad [7]$$

From equation 7, we can conclude that the stimulated emission process shows overall quadratic power depen-

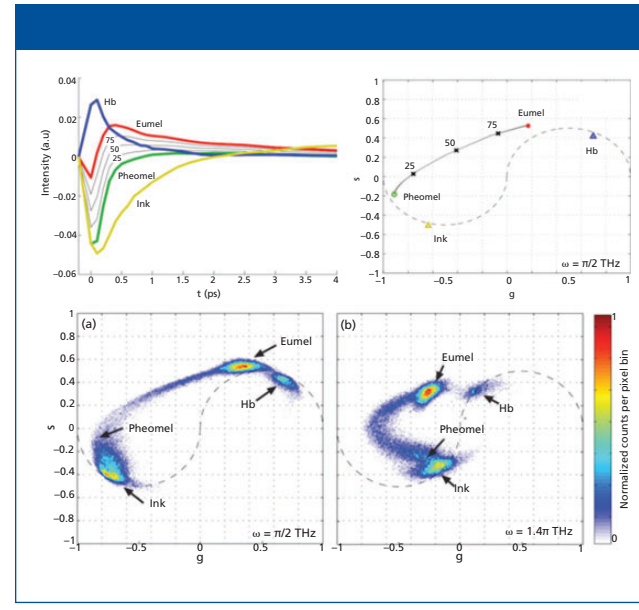

Figure 4: Phasor analysis to interrogate pump–probe signal. Experimental transient absorption spectra of hemoglobin (Hb), sepia eumelanin, syhthetic pheomelanin, and surgical ink (top left). Phasor difference of mixtures of eumelanin and pheomelanin (eumelanin fraction of 75%, 50% and 25%) along with their phasor locations on the s-g coordinate (top right). Cumulative histogram phasor plot of 17 ocular melanoma samples at frequency /2 THz (bottom left) and 1.4 THz (bottom right). Adapted with permission from reference 54.

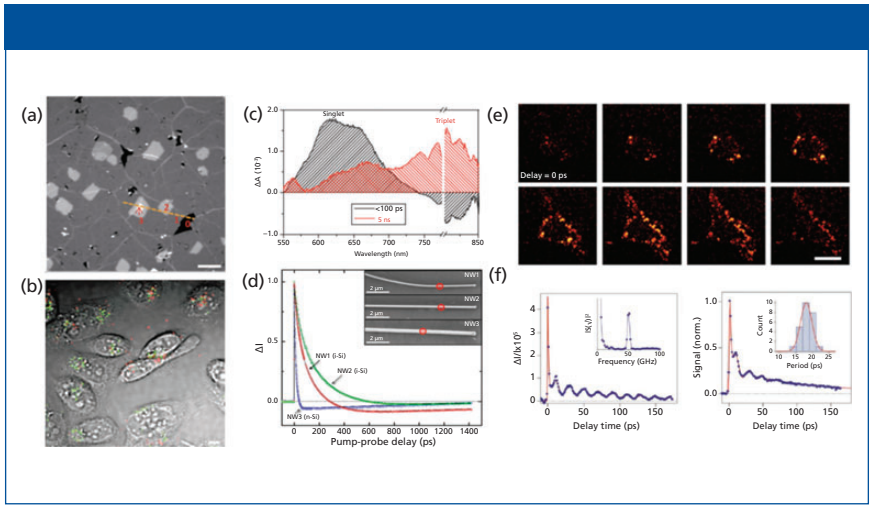

Figure 5: Imaging nanomaterials by pump–probe microscopy. (a) TA imaging of graphene on glass coverslip. 0 stands for defects, 1 is single layer graphene, 2 is double layer, 3 is triple layer, respectively. Pump = 665 nm (1.10 mW) and probe = 820 nm (0.68 mW), respectively. Data adapted from reference 70. (b) Transient absorption image of DNA-SWNTs internalized by CHO cells after 24 h incubation. Gray, transmission of cells; green, S-SWNTs; red, M-SWNTs. Pump = 707 nm, probe = 885 nm. The laser power post-objective was 1 mW for the pump beam and 1.6 mW for the probe beam. Adapted with permission from reference 26. (c) Decay-associated spectra of the triplet (red) and singlet (black) excitons of tetracene obtained by global analysis of the ensemble transient absorption spectra with the probe polarization to maximize triplet absorption. Data adapted from reference 75. (d) Pump–probe microscopy decay kinetics following photoexcitation of a localized region in three different Si nanowires; NW1 (red) and NW2 (green) are intrinsic, and NW3 (blue) is n-type. Curves are fit to a tri-exponential decay. Inset shows the SEM image of three wires. Adapted with permission from reference 76. (e) 3D transient absorption microscopic images of gold nanodiamonds in living cells taken from eight successive focal planes with 1-µm step. Scale bar: 20 µm. Data adapted from reference 77. (f) Transient absorption trace from a single Ag nanocube from a sample with an average edge length of 35.5 ± 3.4 nm (left). The inset shows the Fourier transform of the modulated portion of the data. Ensemble transient absorption trace for the Ag nanocube sample (right). Inset gives a histogram of the measured periods from the single-particle experiments, red line is the distribution calculated from the size distribution of the sample. Adapted with permission from reference 78.

dence, allowing three-dimensional optical sectioning. In addition, the linear dependence upon the concentration of analyte allows for quantitative analysis. The detected sensitivity would be down to 10^{-9} M if the incident irradiance of pump beam and probe beam are in the range of megawatt cm^{-2} (37).

Ground-State Depletion

Ground-state depletion (GSD) microscopy is a form of super-resolution light microscopy suggested almost a decade ago (38), and it was first demonstrated in 2007 (39). Similar to stimulated emission, it presents as an out-phase signal (Figure 1). The overall mechanism is consistent with other transient absorption mechanisms. If expressed in equation form, the GSD process has the same expression as stimulated emission in equation 4. The only difference lies in the probe wavelength. For GSD, the probe is chosen close to the maximal absorption peak, whereas the probe beam in the case of stimulated emission is selected away from the absorption peak.

Based on ground-state depletion, single-molecule detection at room temperature has been achieved (40). Under the condition that both pump and probe beams (continuous-wave lasers) were chosen close to near saturation intensity levels (350 µW at the focus for each beam), a shot noise limited sensitivity is achieved. The detected sensitivity for Atto647N is 15 nM with 1s integration time. The order of modulation depth of the transmitted probe beam by a single molecule (Atto647N) is ~10^{-7}, which means we can still demodulate the signal from a lock-in amplifier. Based on the mechanism above, ground-state depletion microscopy could reach single-molecule detection (40). The ground state depletion method could also be applied to localize fluorescence emission from fluorophores bound to the surface of a nanowire, thus making it possible to map out the structure of a nanowire (41). Zink and colleagues also showed how GSD microscopy can be applied to measure tubulin modifications in epithelial cells (42). High sensitivity coupled with optical sectioning capability makes ground-state depletion microscopy an important emerging technique.

Instrumentation

A typical pump–probe imaging setup is shown in Figure 2. An optical parametric oscillator pumped by a high-intensity mode-locked laser generates synchronous pump and probe pulse trains. The Ti:sapphire oscillator is split to separate pump and probe pulse trains. Temporal delay between the pump and probe pulses is achieved by guiding the pump beam through a computer-controlled delay line. Pump beam intensity is modulated with an acousto-optic modulator (AOM), and the intensity of both beams is adjusted through the combination of a half-wave plate and polarizer. Subsequently, pump and probe beams are collinearly guided into the microscope. After the interaction between the pump beam and the sample, the modulation is transferred to the unmodulated probe beam. Computer-controlled scanning galvo mirrors are used to scan the combined lasers in a raster scanning manner to create microscopic images. The transmitted light is collected by the oil

condenser. Subsequently, the pump beam is spectrally filtered by an optical filter, and the transmitted probe intensity is detected by a photodiode. A phase-sensitive lock-in amplifier then demodulates the detected signal. Therefore, pump-induced transmission changes of the sample versus time delay can be measured from the focus plane. This change over time delay shows different decay signatures from different chemicals, thus offering the origin of the chemical contrast.

Generally speaking, lasers applied in pump–probe microscopy can be divided into two types: systems working with relatively high pulse energy (5–100 nJ) and repetition rate of 1–5 kHz, and systems using a low pulse energy (0.5–10 nJ) and >1 MHz repetition rate (27). With appropriate detection schemes that involve multichannel detection on a shot-to-shot basis, the first type can achieve the signal detection sensitivity of ~10^{-5} units of absorbance over a broad wavelength range (27). Nevertheless, the presence of multiple excited states under high excitation density conditions leads to singlet-singlet annihilation (43). Therefore, this scheme is sensitive to artifacts. The second type with high repetition rates allows for averaging more laser shots per unit time. As a result, the detection sensitivity of ~10^{-6} units of absorbance can be achieved (28). By employing high-frequency (that is, megahertz) lock-in modulation, Hartland and coworkers detected signals from isolated single-walled carbon nanotubes with a sensitivity of $\Delta I/I \sim 5 \times 10^{-7}$ (44). Moreover, in this scheme, the modulation provided by either an AOM or an electro-optic modulator (EOM) operates at a high frequency in the range of 100 kHz to 10 MHz, where the noise approaches the shot noise limit. One possible drawback of such setups is their high probability of detecting the accumulation of long-lived species, such as triplet or charge-separated states (27).

When it comes to the detection of pump–probe signal, a phase-sensitive lock-in amplifier is usually indispensably used to demodulate the probe signal. Slipchenko and colleagues reported a cost-effective tuned amplifier for frequency-selective amplification of the modulated signal. By choosing a pump beam of 830 nm and a probe beam of 1050 nm, the tuned amplifier can be used for pump–probe imaging of red blood cells. This lock-in free method improved the single-to-noise ratio by one order of magnitude compared to conventional detection based on a lock-in amplifier (45).

Spatial resolution is designated as the distance between two points of the sample that can be resolved individually according to the Rayleigh criteria. The lateral (r_0) and axial (z_0) resolutions are defined (46) as

$$r_0 = \frac{0.61 \cdot \lambda}{NA} \text{ and } z_0 = \frac{2 \cdot n \cdot \lambda}{(NA)^2} \quad [8]$$

where λ is the wavelength, n is the refractive index of the medium and NA is the numerical aperture. By using spatially controlled saturation of electronic absorption, diffraction limit in far-field imaging of nonfluorescent species could be broken as shown in Figure 3a. Wang and colleagues designed a doughnut-shaped laser beam to saturate the electronic transition in the periphery of the focal volume, thus introducing modulation only at the focal center. By raster scanning three collinearly aligned beams, high-speed subdiffraction-limited imaging of graphite nano-platelets was achieved (47).

Alternatively, Miyazak and colleagues (48) demonstrated the use of annular beams in pump–probe microscopy to improve spatial resolution in the focal plane, since the point spread function (PSF) in pump–probe microscopy is 23% (43%) smaller than the diffraction-limited spot size of the pump (probe) beam. The authors also used intensity modulated continuous wave laser diodes in a balanced detection scheme to achieve subdiffraction resolution with shot-noise limited sensitivity (49,50).

Regarding the sensitivity, single-

Table I: Applications of pump–probe microscopy

Authors	Topic	Application	References
Muskens et al.	Nanomaterial	Single metal nanoparticle	65
Davydova et al.	Nanomaterial	PtOEP crystal	66
Xia et al.	Nanomaterial	Hot carrier dynamics in HfN and ZrN	67
Cui et al.	Nanomaterial	WSe_2	68
Li et al.	Nanomaterial	Graphene of different layers and defects	70
Gao et al.	Nanomaterial	Hot photon dynamics in graphene	61
Lauret et al. Gao et al. Koyama et al. Ellingson et al. Kang et al.	Nanomaterial	SWNTs	60, 62, 63, 73, 74
Jung et al. Tong et al.	Nanomaterial	Phase of semiconductor-SWNTs and metallic-SWNTs	25, 26
Gao et al.	Nanomaterial	Chirality grown of SWNTs	74
Wan et al.	Nanomaterial	Singlet fission of tetracene	75
Gabriel et al.	Nanomaterial	Carrier motion in silicon nanowires	76
Chen et al.	Nanomaterial	Nonfluorescent nanodiamond	77
Hartland et al.	Nanomaterial	Silver nanocube	78
Lo et al.	Nanomaterial	Single CdTe nanowire	79
Mehl et al.	Nanomaterial	Single ZnO rods	80
Cabanillas et al.	Nanomaterial	Optoelectronic semiconductor	33
Wong et al. Polli et al. Guo et al. Yan et al.	Polymer	Polymer blends	81, 83, 84, 85
Guo et al. Simpson et al.	Semiconducting materials	Perovskite film	69, 82
Fu et al. Min et al.	Hemoglobin	Deep-tissue imaging of blood vessels	36, 37
Fu et al. Piletic et al.	Melanin	Differentiation between eumelanin and pheomelanin	5, 15, 87
Samineni et al.	Historical pigments	Lapis lazuli	19
Villafana et al.	Historical pigments	Quinacridone red and ultramarine blue	20

molecule detection can be achieved through pump–probe microscopy. Chong and coworkers conducted ground-state depletion microscopy and achieved a detection limit of 15 nM with a 1-s integration time, which corresponds to 0.3 molecules in the probe volume, indicating the detection of a single-molecule absorption signal as shown in Figure 3b (40). In their work, the sample was illuminated by two tightly focused laser beams where the pump beam and the probe beam have different wavelengths but both are within the molecular absorption band of the analyzed sample. In this case, the pump beam only excites a molecule so that it only stays in its ground state, and, hence, photons from the probe beam can't be absorbed. Fast on-off modulation of a strong, saturating pump beam leads to the modulation of transmitted probe beam at the same modulation frequency.

Data Analysis Methods

Generally, two methods can be used to analyze a decay curve. The easier method is multiexponential fitting to get the decay constants. However, a drawback is that its accuracy is relatively low. The other method is called phasor analysis, a method that needs neither any assumptions regarding the physical model nor integration fitting to determine the lifetimes of multiexponential signals (51–53). When dealing with a long lifetime (~1 ns), another method that is based on phase information and modulation frequency can be used as is discussed below.

Multiexponential Fitting

Multiexponential fitting, as the name implies, fits the time-resolved curves with an exponential decay model. This method is easy to conduct and understand. The time-resolved intensity is regarded as the conjugation between the instrumental response $R(t)$ and the response from sample $S(t)$:

$$I(t) = \int R(t-t')S(t')dt' \quad [9]$$

Suppose the time resolution of the detector is modeled by a Gaussian function with a full width half maximum as σ:

$$R(t) = A_1 \exp\left(-\frac{t^2}{2 * \sigma^2}\right) \quad [10]$$

In this case, pump–probe decay is modeled by an exponential decay with decay constant τ:

$$S(t) = A_2 \exp\left(-\frac{t}{\tau}\right) \quad [11]$$

Then the convolution integral is

$$I(t) = \exp\left(\frac{\sigma^2}{2\tau^2} - \frac{t}{\tau}\right)\left(1 - erf\left(\frac{\sigma^2 - t * \tau}{\sqrt{2} * \sigma * \tau}\right)\right) \quad [12]$$

where *erf (x)* is the error function, a standard function in most mathematical software packages. For single exponential decay, the mathematical equation for the time-resolved decay curve is

$$I(t) = I_0 + A * \exp\left(\frac{\sigma^2 - 2 * t * \tau}{2 * \tau^2}\right) * \left(1 - erf\left(\frac{\sigma^2 - t * \tau}{\sqrt{2} * \sigma * \tau}\right)\right) \quad [13]$$

where τ is the decay constant and I_0 is the signal from background. A similar equation can be used for double exponential decay. After fitting with this model, we obtain the real decay constant τ along with the laser pulse width σ.

Through the deconvolution approach, we could resolve the time constant purely from decay of chemicals without the effect of laser response function. However, the drawback of this method is that it is sensitive to the initial input parameters, and therefore its accuracy is relatively low.

Phasor Analysis

Phasor analysis is a method that translates the time-resolved decay curve into a single point at a given frequency in the phasor space. One of the most advantageous features of phasor analysis when applied to fluorescent-lifetime imaging microscopy (FLIM) (52,53) is that it has the capability to quantitatively resolve a mixture of fluorophores with different lifetimes. Phasors from those mixtures display linearly across the phasor plot (54). For the first time, Fereidouni and colleagues proved spectral phasor analysis was powerful for the analysis of the fluorescence spectrum at each pixel (55,56). Fu and colleagues further applied this analysis method to hyperspectral stimulated Raman scattering data. It allows the fast and reliable cellular organelle segmentation of mammalian cells, without any a priori knowledge of their composition or basis spectra (57).The basic mechanism for this method is described through mapping the real parts of the signal against the imaginary parts of the signal after Fourier transform of the time-resolved curve:

$$g(\omega) = \frac{\int I(t) \cos(\omega t)\, dt}{\int |I(t)|\, dt} \quad [14]$$

$$s(\omega) = \frac{\int I(t) \sin(\omega t)\, dt}{\int |I(t)|\, dt} \quad [15]$$

Any multicomponent signal can be described as

$$I_{tot}(t) = \sum_i f_i I_i(t) \quad [16]$$

where f_i is the fraction of each independent species contributing to the total signal:

$$g_{tot} = \sum_i f_i \cdot \frac{\int |I_i(t)|\, dt}{\int |I_{tot}(t)|\, dt} \cdot g_i \quad [17]$$

By plotting $g(\omega)$ against $s(\omega)$ at a given frequency, we can map the distribution of different chromophores with distinct lifetimes in the semicircle coordinate. Here ω is a free parameter depending on the separation efficiency. Robles and colleagues demonstrated its capability to discriminate eumelanin, pheomelanin, and ink by phasor analysis as shown in Figure 4 (54).

The phasor representation of lifetime images has become popular because it provides an intuitive graphical view of the fluorescence lifetime content without any prior knowledge. Meanwhile, it significantly improves the overall signal-to-noise ratio when used for global analysis.

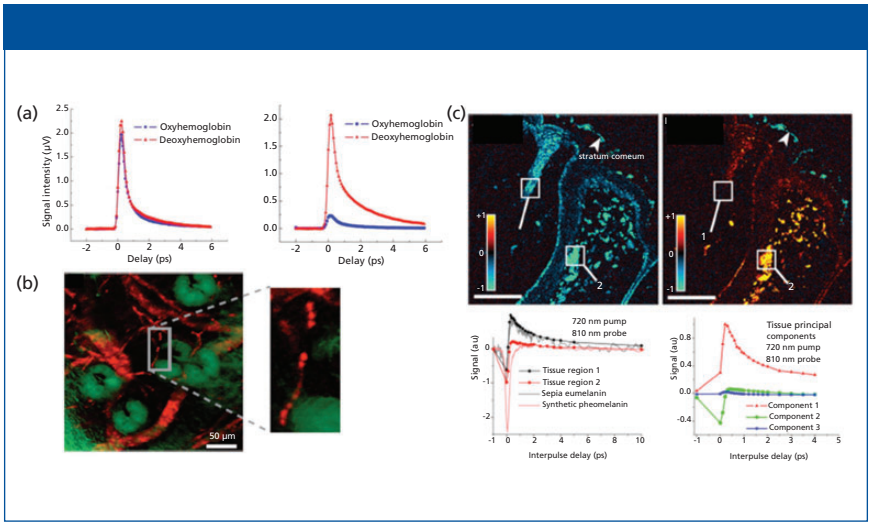

Figure 6: Imaging microvascular and melanomas by pump–probe microscopy: (a) Pump–probe microscopy is applied to differentiate oxyhemoglobin and deoxyhemoglobin. ESA signal from oxyhemoglobin and deoxyhemoglobin with pump = 810 nm (10 mW) and probe = 740 nm (6.4 mW) (left). ESA signal from oxyhemoglobin and deoxyhemoglobin with pump = 740 nm (2.4 mW) and probe = 810 nm (10 mW) (right). Adapted with permission from reference 36 (copyright 2008 Society of Photo-Optical Instruction Engineers). (b) Ex vivo imaging of microvasculature network of a mouse ear based on endogenous hemoglobin contrast. Red, blood vessel network; green, surrounding sebaceous glands. Pump = 830 nm (~20 mW, two-photon excitation of Soret band), probe = 600 nm (~3 mW, one-photon stimulated emission of Q-band of hemoglobin). Adapted with permission from reference 37. (c) Pump-probe image of a compound nevus at 0-fs (left) and 300-fs (right) interpulse delay (top). Regions containing eumelanin have positive signal (red/orange). Pump–probe time delay traces comparing tissue regions of interest 1 and 2 (white boxes in top) with pure solution melanins (bottom). The first three principal components found in tissue pump–probe signals (loadings plot, right). The first two components account for more than 98% of the variance. Pump = 720 nm, probe = 810 nm. Scale bar = 100 μm. Adapted with permission from reference 6.

Besides that, the region of interest selected in the phasor plot can be mapped back to its corresponding image to realize segmentation (56).

Frequency Domain Approach

The frequency domain approach is more suitable for long-lived excited state. In this method, the lifetime information is extracted through a phase-sensitive detection. A simple model tan ϕ = ω * τ is applied to calculate the lifetime on the basis of phase change corresponding to different modulation frequency. When a modulated pump beam $I_1(t) = I_1(1+\cos \omega t)$ is incident on the sample, the excited state population is given by Miyazaki and colleagues (58) in the following equation:

$$P(t) = \frac{\sigma_1 I_1}{h\nu_1 s}\{A(\omega)\cos[\omega t+\phi(\omega)]+1\} \quad [18]$$

where

$$A(\omega) = \frac{1}{\sqrt{1+(\omega * \tau)^2}} \quad [19]$$

$$\phi(\omega) = \tan^{-1}(\omega * \tau) \quad [20]$$

Here, σ_1 is the absorption cross section, ν_1 is the frequency of the pump, h is the Planck constant, s is the beam waist area at the focal point, ϕ is the phase calculated from the x and y channel signals, and τ is the excited-state lifetime. In the case of a long excited-state lifetime, equation 20 suggests an efficient method: tan ϕ = ω * τ. This equation demonstrates the linear relationship between tan ϕ and modulation frequency ω and the corresponding phase images. The slope of this equation yields the lifetime of the excited state. It is worth noting that because of the relatively larger shot noise at lower modulation frequency, the standard deviation is very high (59).

Applications of Pump–Probe Microscopy

With its superior detection sensitivity, chemical specificity and spatial-temporal resolution, pump–probe microscopy has been used to study pigmentation (14), microvasculature (14), ultrafast relaxation in SWNTs (23–26,60–63), single semiconductor and metal nanostructures (64,65), and other nanomaterials (66–69). Table I summarizes representative applications in various areas. These applications are reviewed in more detail in the following sections.

Semiconducting Nanomaterials and Graphene

Pump–probe microscopy provides a vivid image of graphene with high sensitivity. Muskens and colleagues have demonstrated the study of a single metal nanoparticle by combining a high-sensitivity femtosecond pump–probe setup with a spatial modulation microscope (65). Besides metal nanoparticles, Zhang and colleagues also imaged graphene with single-layer sensitivity through transient absorption, whereas other techniques such as high-resolution transmission electron microscopy, scanning electron microscopy, and scanning tunneling microscopy proved to be cumbersome in sample preparation (70). In their work, they achieved high speed (2 μs/pixel) imaging of graphene on various substrates under ambient condition and even in living cells and animals. Interestingly, the intensity of the transient absorption images is found to linearly increase with the number of layers of graphene. In Figure 5a, in the TA image of graphene, we can clearly observe the location of graphene defects and that of different layers. It only takes a few seconds to acquire a TA image of graphene. In addition, with polyethylene glycol used to functionalize graphene oxide, these well-dispersed particles have shown the capability for in vitro and ex vivo imaging in

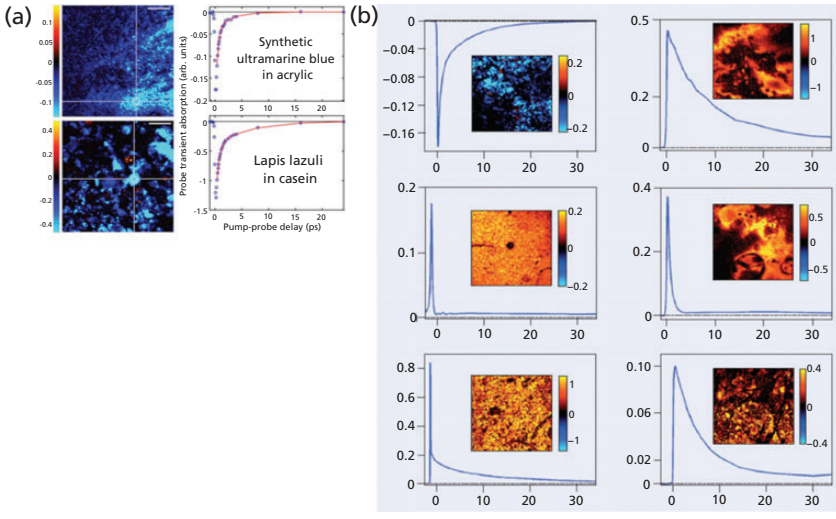

Figure 7: Imaging artistic pigments by pump probe microscopy: (a) Transient absorption images of synthetic ultramarine in acrylic (golden artist colors GMSA 400, top) and lapis lazuli in casein (Kremer pigments 10530, bottom) and the corresponding pump-probe delay traces in the indicated region of interest (white rectangle) where the line indicates double-exponential fits. Scalar bar = 100 µm. S/N = 100. Adapted with permission from reference 19 (copyright 2012 Optical Society of America). (b) Graphs showing pump probe dynamics in test samples with the pigments lapis lazuli, vermilion, caput mortuum, quinacridone, phthaloblue, and indigo. Adapted with permission from reference 21.

Chinese hamster ovary (CHO) cells (70).

Pump–probe microscopy is also exploited to study SWNTs. Carbon nanotubes, especially single-wall carbon nanotubes, have attracted much attention in the last two decades (71,72). The excellent properties of SWNTs in thermal conductivity, electronics, optics, and mechanics make them appealing. Pump–probe microscopy has proved to be a powerful tool to explore the intrinsic photochemical properties of single-wall carbon nanotubes. Accurate detection of carrier dynamics in these nanostructures is essential for understanding and developing their optoelectronic properties. Lauret and colleagues reported for the first time the time-resolved study of carrier dynamics in single-wall carbon nanotubes by means of two-color pump–probe experiments under resonant excitation with a selective injection of energy in the semiconducting nanotubes (73). Jung and colleagues for the first time exploited the phase of the pump–probe signal as a contrast to study SWNTs (25). Later Tong and coworkers showed that transient absorption microscopy offers a label-free approach to image both semiconducting and metallic SWNTs in vitro and in vivo in real time with submicrometer resolution, by choosing appropriate near-infrared wavelengths (26). Semiconducting and metallic SWNTs exhibit transient absorption signals with opposite phases. Figure 5b shows the transient absorption image of DNA-SWNTs internalized by CHO cells, where gray represents the transmission image. The different colors in the image result from different phases representing two different kinds of SWNTs: green represents semiconducting SWNTs and red represents metallic SWNTs. Gao and colleagues reported transient absorption microscopy experiments on individual semiconducting SWNTs with known chirality grown by chemical vapor deposition (CVD) with diffraction-limited spatial resolution and subpicosecond temporal resolution (74)].

Pump–probe microscopy has also

been extensively applied to study nanoparticles and nanowires. Figure 5c presents visualization of singlet fission by observing the decay-associated spectra of the triplet (red) and singlet (green) excitons of tetracene. The curves in Figure 5c were obtained by global analysis of the ensemble transient absorption spectra (75). As shown in Figure 5d, pump–probe microscopy has been used to demonstrate the spatial kinetics of silicon nanowires (76). In addition, nanodiamonds and nanocubes are of great interest to researchers. Figure 5e demonstrates 3D transient absorption microscopic images of gold nanodimonds in living cells (77). Figure 5f shows a fast decay of silver nanocubes resulting from electron-phonon coupling and subsequent modulations from the coherently excited breathing mode (78).

Pump–probe microscopy examines intrinsic excited state dynamics of semiconductors. Lo and colleagues demonstrated transient absorption measurements on single CdTe nanowires, and they showed for the first time that acoustic phonon modes were fast because of the efficient charge carrier trapping at a lower excitation intensity (79). Mehl and coworkers (80) reported pump–probe microscopy of the individual behaviors of single ZnO rods at different spatial locations. Dramatically different recombination dynamics were observed in the narrow tips compared with dynamics in the interior. Cabanillas-Gonzalez and colleagues (33) highlighted the contribution of pump–probe spectroscopy to the understanding of the elementary processes taking place in organic based optoelectronic devices. They further illustrated three fundamental processes (optical gain, charge photo-generation and charge transport). This work opens new perspectives for assessing the role of short-lived excited states on organic device operation. Polli and coworkers developed a new instrument approach by combining broadband femtosecond pump–probe spectroscopy and confocal microscopy, enabling simultaneously high temporal and spatial resolution (81). Guo and colleagues (82) reported spatially and temporally resolved measurements of perovskite by ultrafast microscopy. This work underscores the importance of the local morphology and establishes an important first step toward discerning the underlying transport properties of perovskite materials.

Pump–probe microscopy also provides new insight into the properties of polymer blends by directly accessing the dynamics at the interfacing between different materials (83).Guo and colleagues (84) elucidated the exciton structure, the dynamics, and the charge generation in the solution phase aggregate of a low-bandgap donor-acceptor polymer by transient absorption. The technique enables important applications in controlling morphology. Using ultrafast microscopy, Yan and colleagues proved that adding an amorphous content to highly crystalline polymer nanowire solar cells could increase the performance (85).

Heme-Containing Proteins and Melanins

Responsible for transporting oxygen, hemoglobin is a metalloprotein in the red blood cells of vertebrates. It is an assembly of four globular protein subunits. Each subunit is composed of a protein tightly associated with a heme group. A heme group consists of an iron ion in a porphyrin. It is well known that the heme group portrays strong absorption yet weak fluorescence. These properties make label-free pump–probe microscopy imaging of hemoglobin an ideal approach. Fu and colleagues (36) demonstrated label-free deep tissue imaging of microvessels in nude mouse ear. They chose a pump beam of 775 nm and a probe beam of 650 nm, and successfully harvested two-color TPA images of microvasculature at different depths with a penetration depth of ~70 μm. In their following-up study, they chose a longer probe beam of 810 nm to differentiate oxyhemoglobin and deoxyhemoglobin as shown in Figure 6a. Beyond two-photon absorption, other procedures can also be applied to observe microvessels. Min and colleagues conducted stimulated emission imaging of microvasculature network in a mouse ear based on the endogenous hemoglobin contrast by choosing the pump beam as 830 nm (two-photon excitation of Soret band) and probe beam as 600 nm (one-photon stimulated emission of Q-band) (see Figure 6b) (37).

Pump–probe microscopy could also be used to differentiate different melanins. Melanins generally come in two polymeric forms: eumelanin (black) and pheomelanin (red/brown). Their biosynthetic pathways involve the oxidation of tyrosine leading to the formation of indoles and benzothiazines (87). Pheomelanin is reddish yellow, and it exhibits phototoxic and pro-oxidant behavior (88). Eumelanin is a brown–black pigment that is substantially increased in melanoma. Therefore imaging the microscopic distribution of eumelanin and pheomelanin could be used to separate melanomas from benign nevi in a highly sensitive manner (16). The differences of the signals of these two different melanins are shown in Figure 6c. Eumelanin has an abrupt positive absorption corresponding to excited-state absorption or two-photon absorption, the same as hemoglobin, whereas pheomelanin gives a negative bleaching signal in Figure 6c. Their difference arises from stimulated emission or ground-state bleaching, respectively (6).

Historical Pigments

Pump–probe microscopy could be further exploited to identify pigments in historic artworks. The approach could extract molecular information with high resolution in 3D making it attractive in this application, since accurate identification is of great value for authentication and restoration (19–21). Villafana and colleagues studied the layer structure of a painting by femtosecond pump–probe microscopy, since the variety of pigments in the artist's palate is enormous compared with the biological pigments present in skin (20). This

is a great approach to extract microscopic information for a broad range of cultural heritage applications. Samineni and colleagues (19) were the first to conduct a pump–probe study of lapis lazuli, a semi-precious rock, by analyzing the multiexponential decay behavior as shown in Figures 7a and 7b. The ratio of amplitude for short decay constant to that of long decay constant for the synthetic ultramarine pigment is 6.6 ± 0.35, while that for natural lapis lazuli is 2.5 ± 0.05. Thus, they readily could be distinguished.

Outlook

Looking into the future, we predict the following advancements of this emerging technology. First, compact and low-cost pump–probe microscopy will be developed and made commercially available for broad use of this technique by nonexperts. Second, handheld pump–probe imaging system will be developed to assist precision surgery in the clinic. Third, important applications of pump–probe microscopy will be identified, in which the decay kinetics are used to study cellular development and disease stage. These advances will make pump–probe microscopy an important member of the nonlinear optical microscopy family with broad use in biology, medicine, and materials science.

References

(1) A.H. Zewail, *Science* **242**(4886), 1645–1653 (1988).

(2) D. Zhong et al., *Proc. Natl. Acad. Sci. U.S.A.* **98**(21), 11873–11878 (2001).

(3) S.K. Pal et al., *J. Phys. Chem. B* **106**(48), 12376–12395 (2002).

(4) T. Ye, D. Fu, and W.S. Warren, *Photochem. Photobiol.* **85**(3), 631–645 (2009).

(5) W. Min et al., *Ann. Rev. Phys. Chem.* **62,** 507 (2011).

(6) T.E. Matthews et al., *Science Translational Medicine* **3**(71), 71ra15-71ra15 (2011).

(7) P.A. Elzinga et al., *Appl. Spectrosc.* **41**(1), 2–4 (1987).

(8) T. Katayama et al., Langmuir **30**(31), 9504–9513 (2014).

(9) M. Hu and G.V. Hartland, *J. Phys. Chem. B* **106**(28), 7029–7033 (2002).

(10) G. Seifert et al., *Applied Physics B* **71**(6), 795–800 (2000).

(11) G.V. Hartland, *Chemical Reviews* **111**(6), 3858–3887 (2011).

(12) M.J. Simpson et al., *J. Invest. Derm.* **133**(7), 1822–1826 (2013).

(13) C. Dong et al., *Biophys. J.* **69**(6), 2234 (1995).

(14) D. Fu et al., *J. Biomed. Optics* **12**(5), 054004 (2007).

(15) L. Wei and W. Min, *Anal. Bioanal. Chem.* **403**(8), 2197–2202 (2012).

(16) T.E. Matthews et al., *Biomed. Optics Express* **2**(6), 1576–1583 (2011).

(17) F.E. Robles et al., *Biomed Optics Express* **6**(9), 3631–3645 (2015).

(18) M.J. Simpson et al., *J. Phys. Chem. Letters* **4**(11), 1924–1927 (2013).

(19) P. Samineni et al., *Optics Letters* **37**(8), 1310–1312 (2012).

(20) T.E. Villafana et al., *Proc. Natl. Acad. Sci.* **111**(5), 1708–1713 (2014).

(21) F. Martin, *Physics World* **26**(12), 19 (2013).

(22) S. Link et al., *Phys. Rev. B* **61**(9), 6086 (2000).

(23) L. Huang, H.N. Pedrosa, and T.D. Krauss, *Phys. Rev. Letters* **93**(1), 017403 (2004).

(24) I. Robel, B.A. Bunker, and P.V. Kamat, *Adv. Mater.* **17**(20), 2458–2463 (2005).

(25) Y. Jung et al., *Phys. Rev. Letters* **105**(21), 217401 (2010).

(26) L. Tong et al., *Nat. Nanotech.* **7**(1), 56–61 (2012).

(27) R. Berera, R. van Grondelle, and J.T. Kennis, *Photosynth. Res.* **101**(2-3), 105–118 (2009).

(28) D.Y. Davydova et al., *Laser & Photonics Reviews* **10**(1), 62–81 (2016).

(29) B. Nechay et al., *Rev. Scient. Inst.* **70**(6): p. 2758–2764 (1999).

(30) J. Jahng et al., *Appl. Phys. Lett.* **106**(8), 083113 (2015).

(31) L. Huang and J.-X. Cheng, *Ann. Rev. Mat. Res.* **43**(1), 213–236 (2013).

(32) L. Tong and J.-X. Cheng, *Materials Today* **14**(6), 264–273 (2011).

(33) J. Cabanillas-Gonzalez, G. Grancini, and G. Lanzani, *Adv. Mater.* **23**(46), 5468–5485 (2011).

(34) H.E. Lessing and A. Von Jena, *Chem. Phys. Lett.* **42**(2), 213–217 (1976).

(35) A. Von Jena and H.E. Lessing, *Chem. Phys. Lett.* **78**(1), 187–193 (1981).

(36) D. Fu et al., *J. Biomed. Opt.* **13**(4), 040503

(2008).
(37) W. Min et al., *Nature* **461**(7267), 1105–1109 (2009).
(38) S.W. Hell and M. Kroug, *Appl. Phys. B* **60**(5), 495–497 (1995).
(39) S. Bretschneider, C. Eggeling, and S.W. Hell, *Phys. Rev. Lett.* **98**(21), 218103 (2007).
(40) S. Chong, W. Min, and X.S. Xie, *J. Phys. Chem. Lett.* **1**(23), 3316–3322 (2010).
(41) K.L. Blythe et al., *Phys. Chem. Chem. Phys.* **15**(12), 4136–4145 (2013).
(42) S. Zink et al., *Microscopy Today* **21**(04), 14–18 (2013).
(43) R. van Grondelle, *Biochim. Biophys. Acta.* **811**(2), 147–195 (1985).
(44) B. Gao, G.V. Hartland, and L. Huang, *J. Phys. Chem. Lett.* **4**(18), 3050–3055 (2013).
(45) M.N. Slipchenko et al., *J. Biophoton.* **5**(10), 801–807 (2012).
(46) D.B. Murphy and M.W. Davidson, in *fundamentals of Light Microscopy and Electronic Imaging* (John Wiley & Sons, Inc., 2012), pp. 1–19.
(47) P. Wang et al., *Nature Photonics* **7,** 449–453 (2013).
(48) J. Miyazaki, K. Kawasumi, and T. Kobayashi, *Optics Lett.* **39**(14), 4219–4222 (2014).
(49) E.M. Grumstrup et al., *Chem. Phys.* **458**, 30–40 (2015).
(50) E.S. Massaro, A.H. Hill, and E.M. Grumstrup, *ACS Photonics* **3**(4), pp 501–506 (2016).
(51) G.I. Redford and R.M. Clegg, *J. Fluoresc.* **15**(5), 805–815 (2005).
(52) M.A. Digman et al., *Biophys. J.* **94**(2), L14–L16 (2008).
(53) C. Stringari et al., *Proc. Natl. Acad. Sci.* **108**(33), 13582–13587 (2011).
(54) F.E. Robles et al., *Optics Express* **20**(15), 17082–17092 (2012).
(55) F. Fereidouni et al., *J. Biophoton.* **7**(8), 589–596 (2014).
(56) F. Fereidouni, A.N. Bader, and H.C. Gerritsen, *Optics Express* **20**(12), 12729-12741 (2012).
(57) D. Fu and X.S. Xie, *Anal. Chem.* **86**(9), 4115–4119 (2014).
(58) J. Miyazaki, K. Kawasumi, and T. Kobayashi, *Rev. Scientif. Inst.* **85**(9), 093703 (2014).
(59) D. Fu et al., *J. Biomed. Optics* **13**(5), 054036–054036-7 (2008).
(60) T. Koyama et al., *J. Luminesc.* **169 Part B,** 645–648 (2016).
(61) B. Gao et al., *Nano Lett.* **11**(8), 3184–3189 (2011).
(62) R.J. Ellingson et al., *Phys. Rev. B* **71**(11), 115444 (2005).
(63) S.J. Kang et al., *Nature Nanotechnol.* **2**(4), 230–236 (2007).
(64) M.A. van Dijk, M. Lippitz, and M. Orrit, *Phys. Rev. Lett.* **95**(26), 267406 (2005).
(65) O.L. Muskens, N. Del Fatti, and F. Vallée, *Nano Lett.* **6**(3), 552–556 (2006).
(66) D.Y. Davydova et al., *Chem. Phys.* **464,** 69–77 (2016).
(67) H. Xia et al., *Solar Energy Materials and Solar Cells* **150**, 51–56 (2016).
(68) Q. Cui et al., *ACS Nano* **8**(3), 2970–2976 (2014).
(69) M.J. Simpson et al., *J. Phys. Chem. Lett.* **7**(9), 1725–1731 (2016).
(70) J. Li et al., *Scientific Reports* **5,** 12394 (2015).
(71) M. Terrones et al., *Nature* 3**88**(6637), 52–55 (1997).
(72) A. Bachtold et al., *Science* **294**(5545), 1317–1320 (2001).
(73) J.S. Lauret et al., *Phys. Rev. Lett.* **90**(5), 057404 (2003).
(74) B. Gao, G.V. Hartland, and L. Huang, *ACS Nano* **6**(6), 5083–5090 (2012).
(75) Y. Wan et al., *Nature Chem.* **7**(10), 785–792 (2015).
(76) M.M. Gabriel et al., *Nano Lett.* **13**(3), 1336–1340 (2013).
(77) T. Chen et al., *Nanoscale* **5**(11), 4701–4705 (2013).
(78) G.V. Hartland, *Chem. Sci.* **1**(3), 303–309 (2010).
(79) S.S. Lo et al., *ACS Nano* **6**(6), 5274–5282 (2012).
(80) B.P. Mehl et al., *J. Phys. Chem. Lett.* **2**(14), 1777–1781 (2011).
(81) D. Polli et al., *Advanced Materials* **22**(28), 3048–3051 (2010).
(82) Z. Guo, et al., *Nature Commun.* **6** 7471**(**2015).
(83) C.Y. Wong et al., *J. Phys. Chem. C* **117**(42), 22111–22122 (2013).
(84) Z. Guo et al., *J. Phys. Chem. B* **119**(24), 7666–7672 (2015).
(85) H. Yan et al., *Advanced Materials* **27**(23), 3484–3491 (2015).
(86) D. Fu et al., *Optics Lett.* **32**(18), 2641–2643 (2007).
(87) I.R. Piletic, T.E. Matthews, and W.S. Warren, *J. Chem. Phys.* **131**(18), 181106 (2009).
(88) J.D. Simon et al., *Pigment Cell & Melanoma Research* **22**(5), 563–579 (2009).

Pu-Ting Dong and **Ji-Xin Cheng** are with Purdue University in Indiana. Please direct correspondence to: jcheng@purdue.edu

For more information on this topic, please visit our homepage at: www.spectroscopyonline.com

Recent Advances in Pharmaceutical Analysis Using Transmission Raman Spectroscopy

This article reviews recent advances in the application of transmission Raman spectroscopy (TRS) to pharmaceutical analysis. The TRS technique overcomes subsampling limitations of conventional Raman spectroscopy and enables rapid noninvasive volumetric analysis of intact pharmaceutical tablets and capsules in a quantitative manner with relevance to quality and process control applications. Although only recently introduced to this area, this technique's uptake and breadth of applications are rapidly growing, with regulatory approvals for its use in quality control of manufactured pharmaceutical products recently being granted.

Julia A. Griffen, Andrew W. Owen, Darren Andrews, and Pavel Matousek

In pharmaceutical process and quality control it is often highly desirable to perform rapid quantitative volumetric analysis of tablet and capsule content by intact and noninvasive means without any sample preparation. In this area, transmission near-infrared (NIR) absorption spectroscopy established itself in the last two decades as an effective analytical tool. However, its wider spread is being restricted in part by its limited chemical specificity. This restriction can be lifted in a number of applications by a more recently introduced alternative technique, transmission Raman spectroscopy (TRS). TRS has been demonstrated to provide much higher chemical specificity, which is beneficial particularly in situations involving more-complex formulations. This type of measurement can be accomplished typically with acquisition times of seconds. The ability of the technique to provide well-defined Raman bands easily attributable to individual sample components also aids data interpretation and facilitates means for clearer communication of results to regulatory bodies. Additional advantages of TRS include the ability to probe samples in the presence of water, making the technique also suitable for analyzing slurries and suspensions in aqueous environments (1). On the other hand, the technique can suffer from the inability to probe samples exhibiting excessively high levels of fluorescence; however, this issue can be mitigated by using long laser excitation wavelengths—for example, 830 nm—to minimize the likelihood of electronically exciting fluorophores, which could potentially give rise to excessively high baseline noise within the region of the Raman spectra. Highly absorbing samples at the laser excitation wavelength or Raman emission spectral region (typically ~800–1000 nm) are also inaccessible by this technique although this situation is rather uncommon in drug-product analysis. Excessive heating and thermal damage (burning) could potentially occur with absorbing samples but this heating can be mitigated by using an expanded laser illumination beam (for example 4–8 mm diameter).

Conventional Raman spectroscopy is traditionally performed in backscattering geometry where the Raman signal is collected from within the laser-illuminated zone on the sample's surface. This configuration is unable to probe the entire volume of pharmaceutical tablets or capsules, limiting its use to characterizing near-surface regions of sample around the illumination–collection zone (2,3) (so called *subsampling*), in the absence of coatings or capsules. The advent of TRS, a variant of Raman spectroscopy, where the sample is illuminated over an extended zone on one side and signal collected from the other (see Figure 1), has radically reduced this issue because laser photons propagate via diffusion through the entire body of the sample to be detected on the other side, and, as such, the generated Raman signal conveys information on its volumetric content, although some comparatively small bias toward the center of the tablet and away from sample edges remains (4–6), similar to transmission near-infrared absorption spectroscopy (7).

The transmission Raman concept was demonstrated in the very early days of Raman spectroscopy (8), but until relatively recently its properties and benefits for the noninvasive probing

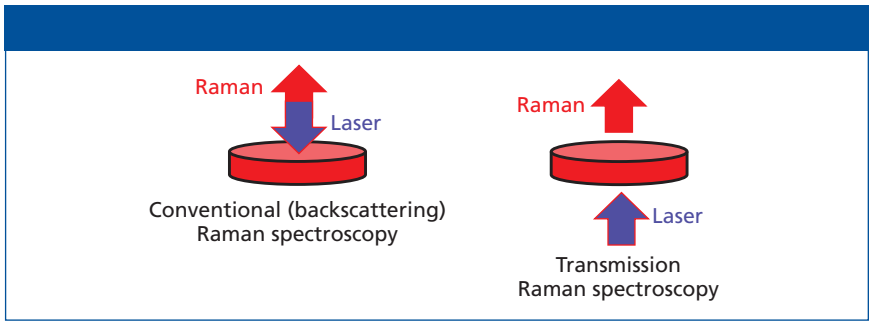

Figure 1: Schematic diagram of conventional and transmission Raman spectroscopy.

of the volumetric content of pharmaceutical samples highlighted in the study of Matousek and Parker (4) followed by other pioneering work (9–11) had not been recognized and exploited in pharmaceutical analysis. The fundamental concept, related methodologies, and early developments of the TRS technique for pharmaceutical analysis is covered in detail in an earlier review (1). Here we focus primarily on more-recent advances of the technique and its applications in pharmaceutical analysis over the past 5 years.

API Quantification

Early proof-of-concept TRS quantification studies (9–11), using less challenging formulations, were followed quickly by more-advanced applications involving more-complex formulations and exploiting a wider range of sample types, which expanded the boundaries of the technique's capability and widened its application space (1). In this area, Lee and colleagues (12) demonstrated that TRS can be successfully applied to the analysis of pharmaceutical formulations in capsules of different colors benefiting from reduced fluorescence background interference from the capsules themselves (13) compared to conventional back-scattering measurements. The team demonstrated that a single calibration model developed from samples held in glass vials could be used to determine active pharmaceutical ingredient (API) concentrations of formulations contained in capsules of different colors, thus avoiding the laborious step of constructing individual models for each capsule color. This benefit was shown by collecting TRS spectra of binary mixtures of ambroxol and lactose in a glass vial and developing a partial least squares (PLS) model for the determination of ambroxol concentration on this set. This model was then directly applied to determining ambroxol concentrations of samples contained in capsules of four colors (blue, green, white, and yellow). Although the prediction performance was slightly degraded when the samples were placed in blue or green capsules because of the presence of residual fluorescence, accurate determination of ambroxol was generally achieved in all cases. The prediction accuracy was also investigated when the thickness of the capsule was varied.

Griffen and colleagues (14) demonstrated that TRS is a viable tool for content uniformity testing of all the constituents of a complex formulation consisting of five components (three APIs and two excipients). The nominal concentration of individual components in this study ranged from 1 to 85% (w/w). The calibration set consisted of 40 tablets and the developed PLS model then successfully predicted all the components in a set of 10 validation tablets covering five sample points. A single PLS model for all components and five individual models each optimized for one component performed similarly and has been used to demonstrate that specificity and robustness of prediction can be achieved through using a robust multifactor orthogonal design-of-experiments approach for calibration samples. The ability to determine multiple analyte concentrations in a single measurement highlights the potential of TRS for assay and content uniformity testing.

To enhance TRS signals and permit further reduction of acquisition times, Griffen and colleagues (15) employed a photon-beam enhancing element (16) before the laser illumination zone to prevent loss of laser radiation from the sample. The study used a five-component formulation. The photon enhancing element permitted improved speed of acquisition by an order of magnitude compared with conventional TRS measurements. The three APIs and two excipients were used with nominal concentrations ranging between 0.4 and 89%. Acquisition times as short as 0.01 s per tablet were reached with acceptable performance for all the sample components. Results suggest that even faster sampling speeds could be achieved for components with stronger Raman scattering cross sections or with higher laser powers. This major improvement in speed of quantification opens exciting prospects for high-throughput TRS in-line analysis in quality control applications within a batch or continuous manufacturing process.

Peeters and colleagues (17) attempted to apply TRS and NIR spectroscopy to the prediction of physical properties of pharmaceutical tablets (as opposed to chemical characterization). Granules were produced on a continuous line by varying granulation parameters. Tableting process parameters were adjusted to obtain uniform tablet weight and thickness. PLS regression was used to correlate spectral information to tablet physical properties (friability, tensile strength, porosity, and disintegration time), but, in this study, no predictive models could be established, which indicated the insensitivity of the methods to these physical properties of sample. This result is in contrast with some earlier studies where such physical properties could be detected in TRS and other data (17). This difference is tentatively attributed to the fact that the previous studies used tablets of varying thickness, whereas in this study the tablet thickness was kept constant (4 mm), suggesting that perhaps tablet thickness variations could be responsible for the earlier observed sensitivity to physical properties of tablets. This hypothesis was not confirmed. Principal component analysis (PCA) was effectively used to distinguish theophylline concentrations and hydration levels and multiple linear regression (MLR) analysis provided insight about how granulation parameters affect granule and tablet properties. All the spectroscopic methods revealed a similar prediction performance with an RMSEP around 1%.

Li and colleagues (18) described the development and validation of a TRS

method using the ICH-Q2 guidance as a template. Niacinamide content in tablet cores was determined in this study. The resultant model statistics were evaluated along with the linearity, accuracy, precision and robustness. Method specificity was demonstrated by accurate determination of niacinamide in the presence of niacin (an expected related substance). The method was demonstrated as fit for purpose with added benefit of very short analysis times (~2.5 s per tablet). The resulting method was used for routine content uniformity analysis of single dosage units in a stability study.

Bilayer Tablets

Zhang and colleagues (19) applied TRS to the quantification of bilayer tablets. This area has so far received only cursory attention and represents an unusually challenging situation. A variety of tablet configurations were examined in this study. A complex spectral response was observed and was effectively modeled using a modified Schrader, Kubelka-Munk model in which both the Raman photon generation factor and photon losses were accounted for. Coupling the results of these studies together yields a comprehensive approach for modeling multicomponent bilayer tablets. The addition of a photon-beam enhancer on the bottom (illumination) surface allowed for a selective over-enhancement of the bottom layer, which aided the analysis of thin layers or coatings.

Quantification of Polymorphs in Pharmaceutical Formulations

Polymorphs are very important in pharmaceutical manufacturing because they determine physiological dissolution rates and their control is therefore often critical. In vibrational spectroscopy, polymorphic forms are best represented by low-wavenumber vibrational (phonon) modes accessible directly by Raman or terahertz spectroscopy. Following an early demonstration of TRS capability in this area by Aina and colleagues (20) to quantify polymorphic content of a binary pharmaceutical formulation, more studies have emerged in this area, setting a clear and important niche for TRS not deliverable by high performance liquid chromatography (HPLC) (where a dissolution step destroys such information) and accessible only partially by NIR, which cannot access phonon modes directly but can sense polymorphs by leveraging changes in overtone and combination bands if such changes are sufficiently pronounced. X-ray diffraction (XRD) is a workhorse here but it also suffers from limited sensitivity and inability to probe the entire sample depth effectively. The availability of the low-wavenumber region simultaneously with the fingerprint region in TRS provides a distinct advantage to TRS over terahertz spectroscopy where only low-wavenumber bands are detected, which therefore enables more straightforward assignment and interpretation of data. Other alternative methods, such as nuclear magnetic resonance (NMR) or differential scanning calorimetry, suffer from limited sensitivity, need sample preparation, or require long data acquisition times.

The first demonstration of TRS for the analysis for polymorphic systems was performed on a binary mixture by Aina and colleagues (20). The study was followed by McGoverin's (21) research performing the quantification of polymorphs in more-complex dosage forms. The efficacy of TRS measurements for the prediction of polymorph content was evaluated using a ranitidine hydrochloride test system. Four groups of ranitidine hydrochloride–based samples were prepared: three containing form I and II ranitidine hydrochloride and microcrystalline cellulose (spanning the ranges 0–10%, 90–100%, and 0–100% form I fraction of total ranitidine hydrochloride), and a fourth group consisting of a form I ranitidine hydrochloride (0–10%)-spiked commercial formulation. Transmission and conventional Raman spectroscopic measurements were recorded from both capsules and tablets of the four sample groups. Prediction models for polymorph and total ranitidine hydrochloride content were more accurate for the tablet than for the capsule systems. TRS was found to be superior to conventional backscattering Raman spectroscopy for the prediction of polymorph and total ranitidine hydrochloride content.

Hennigan and Ryder (22) also carried out a study in which they generated a model tablet system with two excipients at 10% API concentration. The API was a mixture of the FII and FIII polymorphs of piracetam. The formulation was characterized using TRS, conventional backscattering Raman spectroscopy, and NIR spectroscopy. The team demonstrated that it is possible to detect FII polymorph contamination in these model tablets with limits of detection (LODs) of 0.6 and 0.7%, respectively, with respect to the total tablet weight (or ~6–7% of the API content). The TRS method was shown to be the superior method because of its higher speed of analysis (~6 s per sample), better sampling statistics, and the availability of sharper, more-resolved bands in the Raman spectra, which enable easier interpretation of the spectral data. An additional benefit highlighted was the direct access of TRS to the low-frequency (phonon) wavenumber region.

The sensitivity of TRS was further enhanced in a study by Griffen and colleagues (23), who performed a proof of concept study using a commercial TRS instrument with an excitation wavelength of 830 nm, demonstrating the application of TRS to the noninvasive and nondestructive quantification of low levels (0.62–1.32% w/w) of an active pharmaceutical ingredient's polymorphic forms in a pharmaceutical formulation. PLS calibration models were validated with independent validation samples resulting in root mean square error of prediction (RMSEP) values of 0.03–0.05% w/w and a limit of detection of 0.1–0.2% w/w. The study also demonstrated the ability of TRS to quantify all tablet constituents in a single measurement. The team also performed TRS analysis on degraded stability samples for which transformation between polymorphic forms was observed while excipient levels remained constant. Additionally, the authors demonstrated a dramatically enhanced collection speed for TRS measurements by deploying a beam enhancing element that permitted comparable prediction performance at 60 times faster rates (for example, 0.2 s per measurement) than in standard mode.

Vigh and colleagues (24) applied TRS to the estimation of degraded drug percentage, residual drug crystallinity, and glass-transition temperature in the context of melt-extrusion. Tight correlation was shown to exist between the results obtained by confocal Raman mapping and TRS. The investigation of the relationship between process parameters, residual drug crystallinity, and degradation was performed using statistical tools and a factorial experimental design defining 54 different circumstances for the preparation of solid dispersions. Drug content, temperature, and residence time were found to have a significant and considerable effect on the examined factors. By forming physically stable homogeneous dispersions, the originally very slow dissolution of the components was improved, making 3-min release possible in acidic medium.

Determination of Crystalline Content in Amorphous Formulations

Kumar and colleagues (25) investigated the applicability of TRS to characterizing the residual crystallinity in an amorphous material. Amorphous materials are sometime used to enhance oral bioavailability of poorly water-soluble drugs. However, amorphous forms are thermodynamically driven to crystallize to the less soluble forms during processing or storage. Sensitive quantitation of crystallinity is therefore critical in process control and in monitoring the stability and bioavailability of amorphous drug product. The study compared TRS with X-ray powder diffraction and solid-state NMR spectroscopy (ssNMR) approaches to quantification of low levels of crystalline material in an amorphous spray-dried dispersion with a moderate 20% drug load. TRS was demonstrated as a viable alternative for detecting and quantifying the crystalline form of an API in an amorphous solid dispersion. It was shown that TRS has better sensitivity compared to the other techniques with an added benefit of faster acquisition times.

Cocrystals

The high chemical specificity of Raman spectroscopy renders the technique amenable to characterizing more-complex forms of APIs and formulations such as cocrystals. TRS was demonstrated and compared with established technique to be viable to detect cocrystals in a study by Elbagerma and colleagues (26). The study confirmed that TRS is an effective TRS tool to evaluate cocrystal formation through interaction of their components. Burley and colleagues (27) further employed TRS to analyze model formulations comprising tableted cocrystals. The ability of TRS to differentiate between formulations on the basis of both drug loading and drug chemistry (cocrystal versus separate components) was confirmed. It was concluded that TRS allows for fast, automated, unsupervised classification of realistic cocrystal tablet formulations, both in terms of drug loading and in terms of whether two APIs are included as a cocrystal or as separate components. The study also warned that mere visual inspection of data to identify variance and overall data structure could be misleading, and in the concerned study such cursory inspection, in effect, misidentified API chemistry (cocrystal versus "separate components") as the main variance in the data. On the other hand, rigorous quantitative numerical analysis showed that API

content in fact leads to the largest variations between datasets.

Suspensions

Shin and colleagues (28) demonstrated the ability of TRS to assess suspensions with minimal influence from internal particle settling. Because particle concentrations at given points throughout the sample can differ in a partially settled suspension sample, the acquisition of Raman spectra representative of the entire sample composition is critically important for accurate quantitative analysis. The proposed scheme used axially irradiated laser radiation (TRS) in the same or opposite direction of settling, thus allowing laser photons to migrate through the settling-induced particle-density gradient formed in the suspension and to widely interact with particles regardless of their settled locations. As such TRS was expected to be more representative of the overall suspension composition, even with partial settling, compared with conventional localized Raman measurement. The study showed that settling did not significantly degrade the accuracy of the concentration determination, thereby indicating effective acquisition of settling-tolerant TRS spectra.

Recent Advances of the TRS Technique

Following earlier investigations of basic properties of the technique in both the lateral and depth dimensions (29,30), the underpinning TRS technology and understanding of the technique itself have been advancing rapidly. Considerable efforts have been devoted to advances such as boosting signals in Raman spectroscopy, which in general are weaker in TRS geometry than in conventional backscattering Raman configuration. Earlier and subsequent investigations showed that the photon diode concept, which consists of an optical filter placed over an illumination zone and returning laser and Raman photons escaping from the turbid sample back into it, can boost Raman signals in TRS by an order of magnitude (15,16,23). Subsequently, an alternative concept using hemispherical mirrors placed over the illumination zone was demonstrated and investigated by Pelletier (31). This approach was shown to be capable of boosting a TRS signal from a representative commercial pharmaceutical tablet by a factor of 40. These approaches promise to further enhance the potential of TRS by shortening acquisition time and enhancing measurement sensitivity (15,23).

Other methods for enhancing signals include increasing the ability of the Raman detection system to collect more Raman signal from the sample. Because the diffuse TRS signal is spread over a wide area of sample, its collection is highly challenging and in practical scenarios only a small fraction of signal available on sample surface can be collected. The limit is typically set by the signal collection gathering capability of spectrographs (etendue), which represents a bottleneck. Strange and colleagues (32) investigated the use of alternative spectrometer approach based around spatial heterodyne Raman spectrometry (SHRS), which enables them to to achieve potentially much higher etendue values. The SHRS detection concept was applied to measuring TRS spectra of ibuprofen yielding only 2.4

times lower TRS intensity than in backscattering mode. The throughput of the SHRS system was about eight times higher than that of an f/1.8 dispersive spectrometer. However, the signal-to-noise ratio (S/N) was still two times lower for the SHRS than the f/1.8 dispersive spectrometer, apparently because of high levels of stray light. As such, there is the possibility for further improvement of the SHRS technology with a potential to outperform conventional dispersive systems in terms of S/N. Another notable attractive feature of this technology is its potential for miniaturization compared with dispersive spectrometer technology.

Oelkrug and colleagues (33) studied the origins and dependencies of TRS (X_T) and conventional backscattering Raman (X_R) signals both theoretically and experimentally as a function of sample thickness, absorption, and scattering. The study showed that for nonabsorbing layers, the Raman reflection and transmission intensities rise steadily with the layer thickness, starting for very thin layers with the ratio X_T/X_R = 1 and for thick layers, approaching a lower limit of X_T/X_R = 0.5. In stratified systems, Raman transmission allows deep probing even of small quantities in buried layers. In double layers, the information is independent from the side of the measurements. In triple layers simulating coated tablets, the information of X_T originates mainly from the center of the bulk material whereas X_R highlights the irradiated boundary region. However, if the stratified sample is measured in a Raman reflection setup in front of a white diffusely reflecting surface, the study concludes that it is possible to monitor the whole depth of a multiple scattering sample with equal statistical weight. In other words, the approach enables transmission-like measurements from reflectance setups.

Sparen and colleagues (34) investigated the dependence of the accuracy of quantification of TRS signals on matrix properties and compared it with that of NIR spectroscopy. In this work, matrix effects in transmission NIR and Raman spectroscopy were systematically investigated for a solid pharmaceutical formulation varying the factors particle size of the drug substance, particle size of the filler, compression force, and content of drug substance. Principal component analysis of NIR and Raman spectra showed that the drug substance content and particle size, the particle size of the filler, and the compression force affected both NIR and Raman spectra. All factors varied in the experimental design influenced the prediction of the drug substance content to some extent, both for NIR and Raman spectroscopy, with the particle size of the filler having the largest effect. When all matrix variations were included in the multivariate calibrations, however, good predictions of all types of tablets were obtained, for both NIR and Raman spectroscopy. The prediction error using transmission Raman spectroscopy was about 30% lower than that obtained with transmission NIR spectroscopy.

Manufacturing and Regulatory Perspective

Villaumié and colleagues (35) described the application of TRS to manufacturing at Actavis UK Ltd. The company undertook a project to modernize how samples were tested in the QC laboratory and to make significant improvements to the supply chain and speed up the process of product supply to the market. After the researchers reviewed the technologies that can nondestructively test solid oral medicinal products, they identified TRS as the most chemically specific analytical option that avoids subsampling issues from the tablets or capsules; the technique eliminates sample standard preparation time, with routine sample analysis in just minutes, and has an added benefit of eliminating environmental waste. The article describes how approval for the use of TRS as an alternative content uniformity (CU) test was acquired from UK's Medicines and Healthcare Products Regulatory Agency (MHRA). By removing dependence on HPLC, an expensive and time-consuming "workhorse" technique, the company was able to save cost and resources from the QC laboratory and eliminate environmental waste. The study details the method development process—from initial feasibility studies, calibration, and validation to routine use of the model—and describes the regulatory framework for their successful method approval. The company is actively developing additional TRS methods for different solid-dose products with the aim of reducing laboratory costs and time for release of products to the market (36).

Conclusions

The recent advent of TRS for pharmaceutical analysis heralds a new era in intact rapid volumetric analysis of pharmaceutical products in process and quality control. A number of advanced diverse applications have been demonstrated in recent years, including API content uniformity testing of complex formulations, polymorph quantification, and detection and excipient characterization. Beneficial characteristics include experimental simplicity, ease of data interpretation, and the ability to use existing multivariate data analysis tools. Several new regulatory approvals granted recently indicate the initiation of the process of the translation of TRS technology from pharmaceutical R&D laboratories to manufacturing environment.

References

(1) K. Buckley and P. Matousek, *J. Pharm. Biomed. Anal.* **55,** 645–652 (2011).

(2) H. Wang, C.K. Mann, and T.J. Vickers, *Appl. Spectrosc.* **56,** 1538–1544 (2002).

(3) J. Johansson, S. Pettersson, and S. Folestad, *J. Pharm. Biomed. Anal.* **39,** 510–516 (2005).

(4) P. Matousek and A.W. Parker, *Appl. Spectrosc.* **60,** 1353–1357 (2006).

(5) N. Townshend, D. Littlejohn, A. Nordon, M. Myrick, J. Andrews, and P. Dallin, *Anal. Chem.* **11,** 4671–4676 (2009).

(6) J. Johansson, O. Svensson, S. Folestad, A. Sparen, and M. Claybourn, "Transmission Raman Spectroscopy for Robust Tablet Assessment," FACSS Conference Proceedings, Abstract 300 (Louisville, Kentucky, 2009), p. 131.

(7) N. Kellichan, A. Nordon, P. Matousek, D. Littlejohn, and G. McGeorge, *Appl. Spectrosc.* **68,** 383–387 (2014).

(8) B. Schrader and G. Bergmann, *Z. Anal. Chem. Freseniu.* **225,** 230–247 (1967).

(9) J. Johansson, A. Sparen, O. Svensson, S. Folestad, and M. Claybourn, *Appl. Spectrosc.* **61,** 1211–1218 (2007).

(10) C. Eliasson, N.A. Macleod, L.C. Jayes, F.C. Clarke, S.V. Hammond, M.R. Smith, and P. Matousek, *J. Pharm. Biomed. Anal.* **47,** 221–229 (2008).

(11) M. Hargreaves, N.A. Macleod, M.R. Smith, D. Andrews, S.V. Hammond, and P. Matousek *J. Pharm. Biomed. Anal.* **54,** 463–468 (2010).

(12) Y. Lee, J. Kim, S. Lee, Y.-A. Woo, and H. Chung, *Talanta* **89,** 109–116 (2012).

(13) P. Matousek and A.W. Parker, *J. Raman Spectrosc.* **38,** 563–567 (2007).

(14) J. Griffen, A.W. Owen, and P. Matousek, *J. Pharm. Biomed. Anal.* **115,** 277–282 (2015).

(15) J. Griffen, A.W. Owen, and P. Matousek, *Analyst* **140,** 107–112 (2015).

(16) P. Matousek, *Appl. Spectrosc.* **61,** 845–854 (2007).

(17) E. Peeters, A.F. Tavares da Silva, M. Toiviainen, J. Van Renterghem, J. Vercruysse, M. Juuti, J.A. Lopes, T. De Beer, C. Vervaet, and J.-P. Remon, *Asian J. Pharm. Sci.* **11,** 547–558 (2016).

(18) Y. Li, B. Igne, J.K. Drennen, and C.A. Anderson *Int. J. Pharm.* **498,** 318–325 (2016).

(19) Y. Zhang and G. McGeorge, *J. Pharm. Innov.* **3,** 269–280 (2015).

(20) A. Aina, M.D. Hargreaves, P. Matousek, and J.C. Burley, *Analyst* **135,** 2328–2333 (2010).

(21) C. McGoverin, M.D. Hargreaves, P. Matousek, and K.C. Gordon, *J. Raman Spectrosc.* **43,** 280–285 (2012).

(22) M.C. Hennigan and A.G. Ryder, *J. Pharm. Biomed. Anal.* **72,** 163–171 (2013).

(23) J.A. Griffen, A.W. Owen, J. Burley, V. Taresco, and P. Matousek, *J. Pharm. Biomed. Anal.* **128,** 35–45 (2016).

(24) T. Vigh, G. Drávavölgyi, P.L. Sóti, H. Pataki, T. Igricz, I. Wagner, B. Vajna, J. Madarász, G. Marosi, and Z.K. Nagy, *J. Pharm. Biomed. Anal.* **98,** 166–177 (2014).

(25) A. Kumar, L. Joseph, J. Griffen, W. Jenny, T. Chi, Y.J. Hau, M. Bloomfield, P. Matousek, and L. Wigman, *Am. Pharmacetical Rev.* **19**(1),(2016).

(26) M.A. Elbagerma, H.G. M. Edwards, T. Munshi, M.D. Hargreaves, P. Matousek, and I.J. Scowen, *Cryst Growth Des.* **10,** 2360–2371 (2010).

(27) J.C. Burley, A. Alkhalil, M. Bloomfield, and P. Matousek, *Analyst* **137,** 3052-3057 (2012).

(28) K. Shin, P.K. Duy, S. Park, Y.-A. Woo, and H. Chung, *Analyst* **139,** 2813–2822 (2014).

(29) N. Everall, P. Matousek, N. Macleod, K.L. Ronayne, and I.P. Clark, *Appl. Spectrosc.* **64,** 52–60 (2010).

(30) N. Everall, I. Priestnall, P. Dallin, J. Andrews, I. Lewis, K. Davis, H. Owen, and M.W. George, *Appl. Spectrosc.* **64,** 476–484 (2010).

(31) M.J. Pelletier, *Appl. Spectrosc.* **67,** 829–840 (2013).

(32) K.A. Strange, K.C. Paul, and S.M. Angel, *Appl. Spectrosc.* Published online 3702816654156 (2016).

(33) D. Oelkrug, E. Ostertag, and R.W. Kessler, *Anal. Bioanal. Chem.* **405,** 3367–3379 (2013).

(34) A. Sparén, M. Hartman, M. Fransson, J. Johansson, and O. Svensson, *Appl. Spectrosc.* **69,** 580–589 (2015).

(35) J. Villaumie and H. Jeffreys, *Eur. Pharm. Rev.* **20,** 41–45 (2015)

(36) Actavis UK Describes their Regulatory Approval Process for Content Uniformity Testing using Transmission Raman Spectroscopy https://www.cobaltlight.com/news/Actavis-UK-Describes-their-Regulatory-Approval-Process-for-Content-Uniformity-Testing-using-Transmission-Raman-Spectroscopy

Julia A. Griffen, Andrew W. Owen, and **Darren Andrews** are with Cobalt Light Systems Ltd. **Pavel Matousek** is with Cobalt Light Systems Ltd. and the Central Laser Facility at STFC Rutherford Appleton Laboratory on the Harwell Campus (UK). Please direct correspondence to: Pavel.Matousek@stfc.ac.uk ■

For more information on this topic, please visit our homepage at: www.spectroscopyonline.com

Nanoparticles, SERS, and Biomedical Research

In biomedical applications of surface-enhanced Raman spectroscopy (SERS), nanoparticles can enhance the Raman signal and provide additional functionality. Duncan Graham of the University of Strathclyde has been pushing the limits of what can be achieved using functionalized nanoparticles and SERS, in applications such as cholera detection, lipid profiling in cancer cells, and assessing the efficacy of anti-cancer drugs.

You have been using a combination of nanoparticles and SERS in a variety of methods and applications related to biomedical use. What are the various functions that the nanoparticles play?

We use metallic nanoparticles of a variety of different compositions, shapes, and sizes for our research. The most fundamental properties of these nanoparticles is that they enhance Raman scattering and for that purpose, we prefer plasmonic nanoparticles such as silver or gold, although we are well aware of some of the newer nanoparticle materials based on semiconductors that are emerging in the SERS field as alternatives.

When we started in this field over 20 years ago, most of the surface chemistry for SERS had been developed to work with gold nanoparticles. My background, however, was in synthetic chemistry and I was interested in developing robust surface chemistries that worked well with silver nanoparticles, which typically give a larger enhancement of Raman scattering than gold nanoparticles. We have been able to build up a repertoire of ligands and chemistries for functionalization of predominantly silver nanoparticles. We also have started to understand more about the complex surface interactions going on for both gold and silver nanoparticles with a number of target analytes.

So getting to your question, the first function that the nanoparticle displays is enhancing the Raman scattering. The second function we are interested in is using them as a linker; because of their large surface area we can add multiple species to one nanoparticle and effectively view the nanoparticle as a linker between the species and a tag. For instance, a DNA sequence and a strongly scattering molecule such as malachite green isothiocyanate can be added to a nanoparticle in a self assembly process that effectively tags the DNA sequence with the malachite green through a nanoparticle, resulting in a strong SERS signal. The large surface area of the nanoparticle allows us to add multiple molecules per nanoparticle, which is interesting from a delivery perspective but also in terms of looking for cooperative binding effects when targeting weak noncovalent interactions such as antibody–antigen interactions or DNA hybridizations. The third function of the nanoparticles that we are interested in is that they have a plasmonic heating effect when we tune our excitation frequency to match the plasmon of the nanoparticles. We can experience significant heating and by playing with the nanoparticle composition, the molecular functionalization, and the excitation frequencies, we can tune between seeing enhancement of Raman scattering and heating up of the system. By controlling and investigating these three different functions we are able to use our nanoparticle-based approaches in a variety of different applications for biomedical use.

In one application, you have developed silver glyconanoparticles for low volume and rapid detection of cholera toxin B subunits in freshwater using SERS detection (1). Can you explain briefly how this works?

We are very interested in looking at interactions that can aggregate nanoparticles and as a consequence change the degree of enhancement of Raman scattering from molecules attached to the surface of these particles. In preliminary work we had shown how ConA [concanavalin A, a glucose-specific plant lectin] could interact with glucose-functionalized nanoparticles and we could follow this by SERS at very sensitive levels. That wasn't particularly useful, however, so we started to look for other protein–sugar interactions that could still result in a change in nanoparticle aggregation and follow this using SERS.

The cholera toxin B subunit is a pentameric protein that is released by cholera and interacts with ganglioside GM1, which is located in your gut. This is the reason that cholera toxin ends up being nasty to the human system. There had been some previous studies looking at the cholera toxin B subunit interaction with sugar-coated nanoparticles that had only looked at the plasmonic color changes and had used reasonably complex sugar chemistry. The interaction between the ganglioside and the cholera toxin B subunit is quite complex, with a number of different points of contact from the ganglioside, which was always going to be a syn-

thetic challenge. To shortcut this, we came up with two different linking units that made use of the key sugar residues in the ganglioside, namely galactose and sialic acid. By investigating the ratio of sialic acid to galactose on the nanoparticles and also the spacing away from the surface of each residue we were able to develop a functionalized nanoparticle that interacted very accurately with the cholera toxin B subunit, causing aggregation of the nanoparticles, which we could follow by SERS: In other words, as cholera toxin concentration increased we saw an increase in the SERS signal due to aggregation of these functionalized nanoparticles.

What advantages does this approach to detecting cholera offer compared to previous approaches?

At this stage we have just the proof of principle and we know that we can use a handheld portable Raman system that runs on batteries, meaning that the field portability of this system is very compelling. The cost of such a system is reasonable; however, we still have significant work to do before this becomes a field-deployable SERS detection system.

What challenges remain to make this approach practical for use with patient samples?

This approach was developed predominantly for testing of water samples in areas affected by cholera or potentially affected by cholera. For medical diagnostics, we are using a similar approach but not in solution, rather using a stationary phase and a capture approach, where we can look for either bacteria or micro RNA sequences indicative of disease. This work is still in its infancy but is showing significant promise in moving from a high-performance-instrument–based assay to a point-of-use assay for a specific diagnostic.

You are currently working on lipid profiling in cancer cells using nanoparticles and SERS for purposes such as assessing the effect of anti-cancer drugs. How does this approach work?

The lipid profiling work is pretty new for us and we are seeing some excellent results when comparing normal back scattered Raman mapping of cells with CARS [coherent anti-Stokes Raman spectroscopy] imaging and also we have started to look at anti-cancer drugs with nanoparticles. This work allows us to show cellular structure and molecular changes in an image based on the scattering intensity arising from the lipids and proteins. We are also starting to follow the drug attached to the nanoparticle using the enhanced Raman scattering of the drug. Drug concentrations are typically pretty low inside single cells, hence the use of nanoparticle to enhance the SERS signal, which allows us to follow the movement of the drug–nanoparticle conjugate as well as to produce three-dimensional images with point of reference to the higher concentration signals from the cellular cytoskeleton such as the lipid membranes and proteins.

What are the main challenges you have to overcome to make this approach work?

The main challenge here is to understand the specific lipids, which we see from broad signals and which can contain multiple species in the Raman scattering, and also how to accurately assess the change in IC_{50} [which is a measure of drug efficacy] as a result of the effect of drugs when they are attached to nanoparticles. This is not a trivial challenge and we need to understand more about drug efficacy when the drug is attached to the nanoparticles. The important thing as well is not just to look at the efficacy of the drug but to understand more about changes in molecular composition of the cell, which is where the Raman scattering comes in. Coupled with that we need to understand which specific molecules and which specific lipids are changing in terms of being either up- or down-regulated by synthetic pathways.

What have you been able to achieve so far?

We have several three-dimensional images where we can see our specific drug added to the nanoparticle inside a cancer cell and we can see where this is located. We have started to understand the change in lipid biosynthesis as a whole within cells when anticancer drugs have been added to them. It is incredibly complex but our collaborators in the cancer research fields are pretty excited about the amount of data and the challenge ahead of interpreting this in a meaningful fashion.

You have also been developing a type of nanoparticle to enhance SERS called "nanostars." What are nanostars and how do they work?

Nanostars are three-dimensional particles that have prongs extended from the surface and give rise to very strong scattering of light from the surface. The nanostars can be produced in a number of different ways from either silver or gold and can be produced with tunable plasmon responses from the visible to the near infrared. Many other groups are working on using nanostars for SERS and other applications. Where I think we differ slightly is that we have been looking at the chemistry of the nanostar synthesis coupled with the SERS detection and subsequent properties in a bit more detail, which appears to be giving us some significant control over their stability and reproducibility as well as the degree of enhancement from the system that we are investigating.

Reference

(1) J. Simpson, D. Craig, K. Faulds, and D. Graham, *Nanoscale Horiz.* **1,** 60 (2016). DOI: 10.1039/c5nh00036j

This interview has been edited for length and clarity. To read the full interview please visit: http://www.spectroscopyonline.com/nanoparticles-sers-and-biomedical-research ■

Duncan Graham is the research professor of chemistry and head of department for pure and applied chemistry at the University of Strathclyde in Glasgow. He obtained his BSc Honours in Chemistry from the University of Edinburgh in 1992 and his PhD in bioorganic chemistry in 1996 He is a cofounder and director of Renishaw Diagnostics Ltd. (formerly D3 Technologies Ltd.), which formed in 2007.

A New Mass Spectrometry Method for Protein Analysis

Proteomics and structural biology require specialized mass spectrometry methods for characterizing protein structures and conformations. Jennifer S. Brodbelt, a professor of chemistry at the University of Texas at Austin, focuses on the development and application of photodissociation mass spectrometry for studying biological molecules such as peptides, proteins, nucleic acids, oligosaccharides, and lipids. She recently spoke with *Spectroscopy* about her work with this technique. She is the winner of the 2017 ANACHEM Award, which will be presented at the SciX meeting in October 2017. The award is presented annually to an outstanding analytical chemist based on activities in teaching, research, administration, or other activities that have advanced the art and science of the field.

Your group has developed a new tandem mass spectrometry (MS/MS) method called ultraviolet photodissociation (UVPD) for cleaving proteins into diagnostic fragment ions in the mass spectrometer (1). Can you please briefly describe the basic principles of this approach?

UVPD entails irradiating ions with UV photons inside the mass spectrometer. The ions may absorb one or more photons, a process that deposits considerable internal energy into the ions and which ultimately leads to cleavage of bonds and production of fragment ions. The fragment ions create a diagnostic pattern that serves as a fingerprint of the original structure of the molecule. In short, UVPD is an MS/MS process akin to conventional collisional activation methods, but the process uses photons rather than collisions to energize the ions. Using UV photons leads to significantly higher energy deposition than collisional methods, and typically this means that the resulting spectra will have a larger array of fragment ions and thus give greater confidence in characterizing the structures of molecules. We have used this method to examine many types of molecules ranging from peptides to lipids to nucleic acids to intact proteins.

What are the advantages of the UVPD technique compared with other MS methods for probing protein structures?

One primary advantage is the higher energy deposition of UVPD compared to collisional activation methods. This results in access to a greater range of fragmentation pathways and richer MS/MS spectra. This can be beneficial when trying to characterize isomeric structures or trying to pinpoint structural modifications. We have more recently obtained evidence that the UVPD process may also be sensitive to tertiary structural features of proteins, thus allowing a means to probe protein conformations.

What are its limitations?

First, UVPD is only successful if the ion of interest absorbs UV photons. For example, 193-nm photons are efficiently absorbed by the amide backbone of proteins and peptides. Second, using high-energy UV photons (such as ones at 193 nm) creates extensive fragmentation via multiple pathways. This means that the ion current is dispersed among many fragment ions, ultimately reducing the abundances of ions. Third, using higher laser powers or photon fluxes increases the chances for multiphoton absorption and increases the probability that fragment ions themselves will absorb photons and undergo secondary fragmentation. This process may lead to disintegration of ions or unusual internal ions that are difficult or impossible to assign.

A second publication from your group describes the use of the technique for studying protein–ligand interactions in native-like ternary protein complexes, namely dihydrofolate reductase (DHFR) complexes with a cofactor and with a drug (2). What makes DHFR a good candidate for examination using the UVPD approach?

DHFR is a great candidate for the UVPD approach for several reasons. First, it is a moderately sized protein (<20 kDa), and this is an ideal size for MS/MS characterization of intact proteins. Second, DHFR has tremendous biological importance because of its key role in the folate cycle that produces thy-

mine, a small molecule critical for proliferation of cells. Third, DHFR is known to bind cofactor NADPH and inhibitor methotrexate, thus allowing the characterization of the resulting noncovalent complexes by UVPD-MS. These noncovalent complexes can be transferred to the gas-phase by electrospray ionization and then fully characterized by UVPD-MS.

Your group has recently extended use of the UVPD method to study multiprotein complexes and secondary protein topology (3). Did you encounter any special challenges related to analyzing these larger structures?

Increasing the size of proteins or protein complexes creates unique challenges. The intact masses of these species are larger, so this taxes the performance of many mass spectrometers. At the same time, the range of potential fragment ions (and their charge states) increases with the size of the protein or protein complex, which further complicates assignment of the resulting mass spectra.

What are the next steps in your research?

We are extending the UVPD-MS method for characterization of even larger multimeric complexes and are trying to extend the *m/z* range for analysis of other larger individual proteins by UVPD-MS. We also recognize the importance of mapping modifications of proteins, and that is an objective where UVPD can really shine.

References

(1) J.B. Shaw, W. Li, D.D. Holden, Y. Zhang, J. Griep-Raming, R.T. Fellers, B.P. Early, P.M. Thomas, N.L. Kelleher, and J.S. Brodbelt, *J. Am. Chem. Soc.* **135,** 12646–12651 (2013).

(2) M.B. Cammarata, R. Thyer, J. Rosenberg, A. Ellington, and J.S. Brodbelt, *J. Am. Chem. Soc.* **137,** 9128–9135 (2015).

(3) L.J. Morrison and J.S. Brodbelt, *J. Am. Chem. Soc.* **138,** 10849–10859 (2016). ■

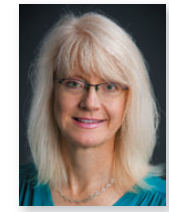

Jennifer S. Brodbelt is the Norman Hackerman Chaired Professor of Chemistry at the University of Texas at Austin. She earned her BS degree in chemistry at the University of Virginia and her doctorate in chemistry at Purdue University under the supervision of Professor Graham Cooks. After a post-doctoral position at the University of California at Santa Barbara, she began her academic career at the University of Texas. Her research interests focus on the development and application of photodissociation mass spectrometry for characterization of the structures and modifications of biological molecules, including peptides, proteins, nucleic acids, oligosaccharides, and lipids.

PRODUCTS & RESOURCES

Raman spectrometer

B&W Tek's iRaman Pro ST portable Raman spectrometer is designed to measure through a variety of materials. According to the company, the spectrometer can measure through clear or semitransparent containers, white and red plastics, pill coatings, yellow and manila colored paper, white packaging envelopes, and glass.

B&W Tek,
Newark, DE;
www.bwtek.com

Raman imaging software modules

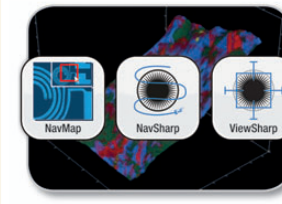

HORIBA Scientific's EasyNav software modules are designed to enable Raman users to navigate images while remaining in focus. According to the company, NavMap, a video feature, shows the global sample and zoomed region of interest within the sample, simultaneously, in real-time; NavSharp provides real-time navigation on a sample image with any topography; and ViewSharp constructs an image in which all surfaces are in focus simultaneously and creates a 3D topography image.

HORIBA Scientific, Edison, NJ; www.horiba.com/scientific

Miniature spectrometer

The Ocean FX miniature spectrometer from Ocean Optics is designed to provide acquisition speed up to 3000 scans per second and onboard buffering to ensure data integrity during reaction monitoring. According to the company, the spectrometer is suitable for sorting and grading in production environments, measurement of transient events, and reaction kinetics monitoring for drug development and similar applications.

Ocean Optics, Dunedin, FL; www.oceanoptics.com

External integrating sphere accessory

PIKE's external integrating sphere accessory, which uses the external beam of the spectrometer, is designed for the analysis of large samples. The accessory provides additional sampling space by positioning samples underneath the sphere for precise reflectivity measurements. According to the company, the internal optics of the external integrating sphere focus the IR beam into a 4-in. diffuse gold-plated integrating sphere.

PIKE Technologies, Madison, WI; www.piketech.com

EDXRF spectrometer brochure

An updated brochure from Rigaku describes the company's NEX DE VS direct excitation EDXRF spectrometers. According to the company, the 10-page document provides an overview of the spectrometer's capabilities, basic specifications, and application options.

Applied Rigaku Technologies, Inc.,
Austin, TX;
www.RigakuEDXRF.com

Liquid flow cells

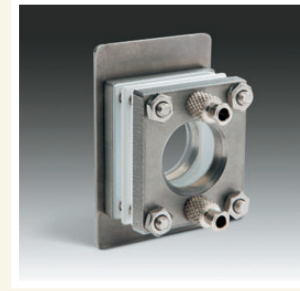

Spectral Systems' Super-Sealed liquid flow cells are designed and manufactured for continuous flow infrared transmission sampling applications. According to the company, the large port diameter permits higher flow rates to speed feedback of component concentration.

Spectral Systems
Hopewell Junction, NY;
www.spectral-systems.com

Deep UV certified reference material

A certified reference material (CRM) from Starna Scientific is designed to qualify a UV spectrophotometer in the deep UV. According to the company, the CRM can provide reliable qualification data below 200 nm, and a new reference material (TS8) was developed with suitable spectral characteristics in the region of 190–230 nm.

Starna Cells, Inc.,
Atascadero, CA;
www.starna.com

Laser metals analyzer

The WITec TrueSurface optical profilometer is designed to enable topographic Raman imaging on rough and uneven samples. According to the company, a new option allows Raman spectra to be acquired from precisely along a surface, or at a set, user-defined distance from a surface.

WITec GmbH,
Ulm, Germany;
www.witec.de

VUV and UV coatings

Broadband VUV and UV coatings from Acton Optics & Coatings are designed to provide reflectance down to 120 nm, with broadband reflectance throughout the visible and near-infrared ranges. According to the company, the coatings are suitable for DUV spectrophotometers, ellipsometry, VUV- and UV-based analytical instrumentation, ICP spectrometers, and aerospace applications.

Princeton Instruments,
Acton, MA;
www.actonoptics.com/products/al-mgf2-mirrors

Silicon drift detector

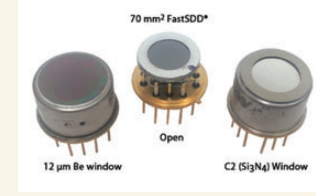

Amptek's Fast SDD-70 detector reportedly combines its silicon drift detector (SDD) and its largest detector in a TO-8 package. According to the company, the SDD has a 70-mm^2 active area collimated to 50 mm^2 and is capable of over 2,000,000 CPS, its resolution is 123 eV FWHM at 5.9 keV, and its peak-to-background ratio is 26,000:1. Applications include benchtop and handheld XRF analyzers, on-line process control, and X-ray sorting machines.

Amptek Inc., Bedford, MA;
www.amptek.com

ICP-OES system

The Agilent 5110 ICP-OES system is designed for analysis in food, environmental, and pharmaceutical testing as well as for mining and industrial applications. According to the company, the system captures axial and radial views of the plasma in a single measurement.

Agilent Technologies,
Santa Clara, CA;
www.agilent.com

Raman analyzer

The RamanRXN2 Multichannel analyzer from Kaiser is designed to provide high-resolution, research-grade Raman spectra on a portable platform for process development monitoring and control. According to the company, a single analyzer can collect Raman data from four channels, addressable by fiber-optic probes capable of direct in situ liquid or solid measurements in applications ranging from from raw materials identification to process control in a manufacturing environment.

Kaiser Optical Systems, Inc.,
Ann Arbor, MI;
www.kosi.com

Pharmaceutical analyzer

Renishaw's RA802 Pharmaceutical Analyser benchtop Raman imaging system is designed for use in the pharmaceutical industry. According to the company, the Raman imaging system enables users to formulate tablets efficiently by speeding up the analysis of tablet composition and structure.

Renishaw,
Hoffman Estates, IL;
www.renishaw.com/Raman

Portable Raman spectroscopy system

The portable StellarCASE-Raman system from StellarNet is designed for material identification and composition analysis using Raman spectroscopy, and is suitable for applications in forensics, anti-counterfeiting, and enhanced Raman spectroscopy. According to the company, the system uses free SpectraWiz ID software to build and search a library for any application.

StellarNet, Inc.,
Tampa, FL;
www.StellarNet.us

NIR spectral sensor

Si-Ware's NeoSpecta Micro near-infrared spectral sensor is designed with a spectral range of 1250–2500 nm with resolution down to 8 nm. According to the company, the sensor allows measuring samples in different form factors including particles, flat surfaces, and ground samples, with no need for sample preparation.

Si-Ware Systems,
Flintridge, CA;
www.neospectra.com

Raman software module

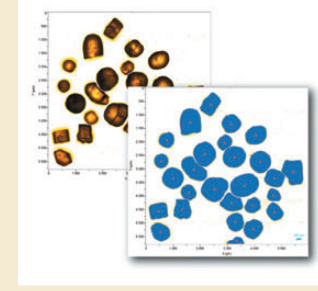

HORIBA Scientific's ParticleFinder module for its LabSpec 6 Spectroscopy software is designed for use with the company's Raman microscopes. According to the company, the module is suitable for automated molecular analysis in pharmaceutical materials, trace forensic evidence, geological rock and mineral particles, and contaminants trapped on filters.

HORIBA Scientific,
Edison, NJ;
www.horiba.com/scientific

Ad Index

ADVERTISER	PG#
Acton Optics & Coatings	23
Amptek	5
B&W Tek, Inc	21
Cannabis Science Conference	50
FACSS	47
Hitachi High Technologies America, Inc	27
HORIBA Scientific	CV4
Kaiser Optical Systems, Inc	39
Mightex Systems	4
Moxtek, Inc	7
New Era Enterprises, Inc	50
Newport Corporation	31, 35
Ocean Optics, Inc	CV2
Ondax	43
PerkinElmer Corporation	3, 9
PIKE Technologies	10
Renishaw, Inc	6
Rigaku GMG	13
Si-Ware Systems	25
Specac	CV3
Spectral Systems	17
Starna Cells, Inc	4, 36
StellarNet, Inc	29
TechnoSpex Pte Ltd	15
TSI, Inc	33
WITec GmbH	41

Specac
brilliant spectroscopy™

PEARL™ IR LIQUID CELL

- analyze various liquids, viscous or aqueous
- change pathlength & window material easily
- avoid fringing patterns with a wedged cell
- attain higher spectral resolutions than ATR

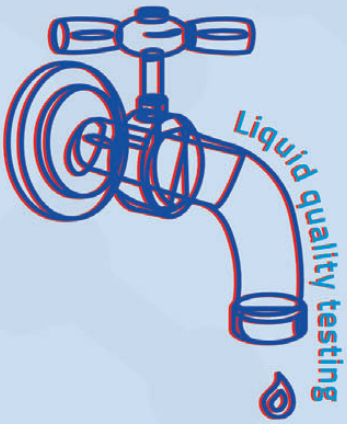

Brilliant Spectroscopy Solutions

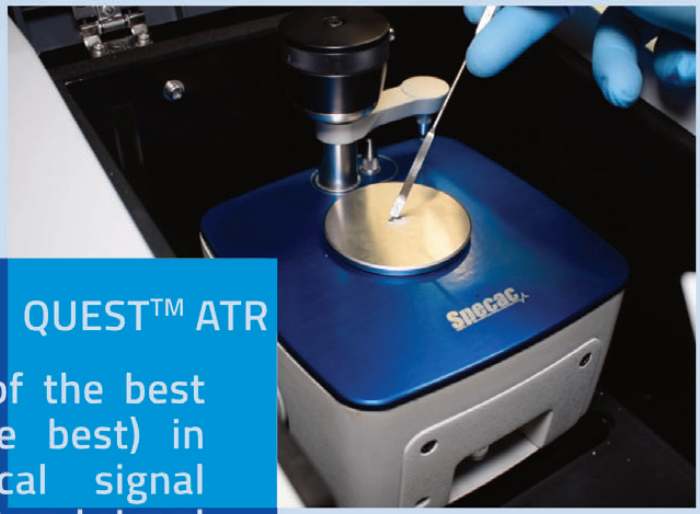

QUEST™ ATR

"One of the best (if not the best) in high optical signal throughput and signal to noise ratio."

A. Stolov
OFS Fitel LLC

Specac Ltd @Specac

www.specac.com sales@specac.com UK: +44 (0)1689 892902 USA: +1 866 726 1126

HORIBA
Scientific

Fluorescence...in the blink of an eye.

Fluorolog® Ultrafast CCD-based fluorometer

The fastest, highest S/N steady state fluorometer in the world!

Fluorolog Ultrafast has the equivalent scan speed of 1,000,000 nm/second and the high quantum efficiency of a CCD out to 1 µm! Designed and built by HORIBA Scientific, it's a fully integrated system, controlled by our FluorEssence® software.

Contact us to step up to the power of instantaneous fluorescence.

ELEMENTAL ANALYSIS
FLUORESCENCE
GRATINGS & OEM SPECTROMETERS
OPTICAL COMPONENTS
FORENSICS
PARTICLE CHARACTERIZATION
RAMAN
SPECTROSCOPIC ELLIPSOMETRY
SPR IMAGING

JOBIN YVON Technology

www.horiba.com/scientific
email: adsci-specty@horiba.com

Explore the future

Automotive Test Systems | Process & Environmental | Medical | Semiconductor | Scientific

HORIBA